nature materials

ARTICLES

https://doi.org/10.1038/s41563-019-0546-6

Taxanes convert regions of perturbed microtubule growth into rescue sites

Ankit Rai[1], Tianyang Liu[2], Simon Glauser[3], Eugene A. Katrukha[1], Juan Estévez-Gallego[4], Ruddi Rodríguez-García[1], Wei-Shuo Fang[5], J. Fernando Díaz[4], Michel O. Steinmetz[6,7], Karl-Heinz Altmann[3], Lukas C. Kapitein[1], Carolyn A. Moores[2] and Anna Akhmanova[1*]

Microtubules are polymers of tubulin dimers, and conformational transitions in the microtubule lattice drive microtubule dynamic instability and affect various aspects of microtubule function. The exact nature of these transitions and their modulation by anticancer drugs such as Taxol and epothilone, which can stabilize microtubules but also perturb their growth, are poorly understood. Here, we directly visualize the action of fluorescent Taxol and epothilone derivatives and show that microtubules can transition to a state that triggers cooperative drug binding to form regions with altered lattice conformation. Such regions emerge at growing microtubule ends that are in a pre-catastrophe state, and inhibit microtubule growth and shortening. Electron microscopy and in vitro dynamics data indicate that taxane accumulation zones represent incomplete tubes that can persist, incorporate tubulin dimers and repeatedly induce microtubule rescues. Thus, taxanes modulate the material properties of microtubules by converting destabilized growing microtubule ends into regions resistant to depolymerization.

Microtubules are cytoskeletal filaments essential for numerous cellular functions. They are formed by the polymerization of tubulin dimers into a regular lattice[1]. Microtubule lattices display structural plasticity, which means that they can adopt multiple conformational states with varying protofilament arrangements, curvature and extent of tube closure[2,3]. Transitions between these states can be controlled by the nucleotide state of tubulin, by tubulin isoforms and modifications, and by local mechanical strain and binding of proteins and drugs[2–4].

Taxol (the brand name of the drug paclitaxel) is a microtubule-targeting agent (MTA) that is widely used for cancer therapy[5–7]. Taxol stabilizes microtubules by binding to a luminally exposed β-tubulin site that is shared by other microtubule-stabilizing agents[6–8]. Taxol has been shown to straighten individual microtubule protofilaments[9], and cryo-electron microscopy (cryo-EM) analysis indicated that Taxol allosterically affects longitudinal interfaces between tubulin dimers by counteracting microtubule lattice compaction induced by guanosine triphosphate (GTP) hydrolysis[10–12]. Furthermore, analysis of MTA interactions with unpolymerized tubulin showed that some taxane-site ligands, such as epothilone A, affect the structure of the β-tubulin M-loop, which contributes to the lateral interactions between tubulin dimers[13–15]. The notion that taxane-site binding compounds stabilize lateral tubulin interactions is supported by a recent cryo-EM study[16]. While such structural insights explain how these MTAs stabilize microtubules at saturating (micromolar) concentrations, they do not account for the drug effects at lower concentrations, which potently suppress both microtubule growth and shortening[5]. Understanding such effects is of crucial importance, because they represent the clinically relevant situation as the concentration of Taxol in plasma during chemotherapy was estimated to be in the range between tens and a few hundred nanomolar (nM)[17–20].

Our previous work has shown that non-saturating Taxol concentrations (50–100 nM) can promote catastrophes in vitro by the End Binding (EB) family proteins[21]. Catastrophe potentiation by low Taxol concentrations is readily observed in cells (for an example, see ref. [22]). In line with these data, low concentrations of Taxol and microtubule-destabilizing vinca alkaloids synergize rather than counteract each other in inhibiting cancer cell proliferation[23], in spite of having seemingly opposite mechanisms of action. Low Taxol concentrations thus do not increase overall microtubule stability; however, they do cause formation of discrete sites that block microtubule shrinkage and induce repeated rescues[21]. To understand how such rescue sites are formed, we visualized drug binding during microtubule growth using fluorescent taxane-site ligands. We found that these MTAs cooperatively bind to microtubule tips that are in a pre-catastrophe state and convert them into islands of stabilized microtubule lattice.

Taxane accumulations induce microtubule rescues

For direct visualization of the effects of taxanes on microtubule dynamics, we used two green fluorescent Taxol derivatives, Fchitax-3 and Flutax-2 (refs. [24,25]) (Supplementary Fig. 1a). We used a total internal reflection fluorescence (TIRF) microscopy-based assay, in which microtubule seeds stabilized with the slowly hydrolysable GTP analogue guanosine-5′-[(α,β)-methyleno]triphosphate, sodium salt (GMPCPP) are extended in the presence of soluble tubulin with or without other proteins or drugs[21,26] (Supplementary Fig. 1b,c). Whereas almost no rescues occurred either with tubulin alone or in the presence of mCherry-EB3, we observed frequent

[1]Cell Biology, Neurobiology and Biophysics, Department of Biology, Faculty of Science, Utrecht University, Utrecht, the Netherlands. [2]Institute of Structural and Molecular Biology, Birkbeck, University of London, London, UK. [3]Department of Chemistry and Applied Biosciences, Institute of Pharmaceutical Sciences, ETH Zürich, Zurich, Switzerland. [4]Chemical and Physical Biology, Centro de Investigaciones Biológicas, Consejo Superior de Investigaciones Científicas, Madrid, Spain. [5]State Key Laboratory of Bioactive Substances and Functions of Natural Medicines, Institute of Materia Medica, Beijing, China. [6]Laboratory of Biomolecular Research, Division of Biology and Chemistry, Paul Scherrer Institut, Villigen, Switzerland. [7]University of Basel, Biozentrum, Basel, Switzerland. *e-mail: a.akhmanova@uu.nl

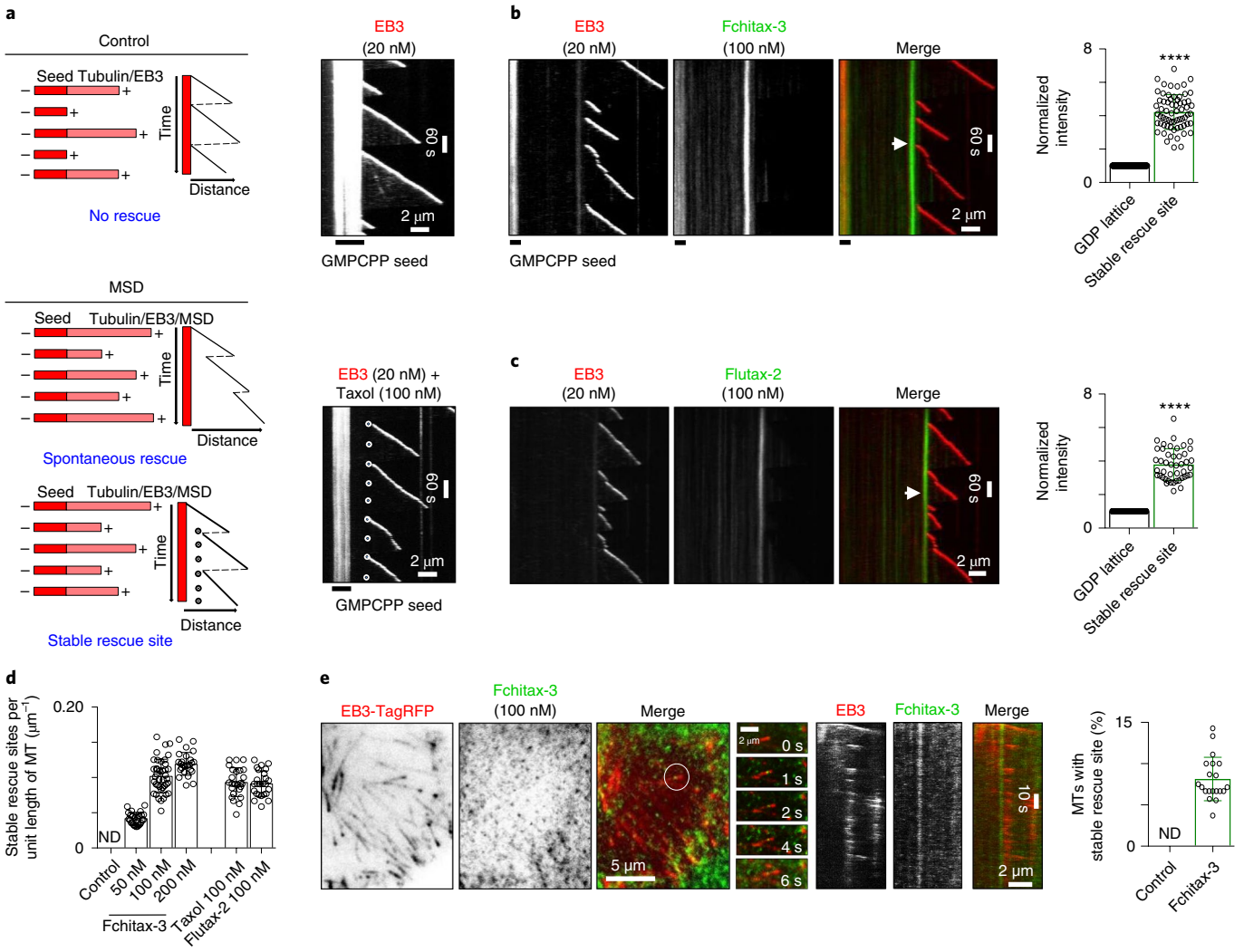

Fig. 1 | Taxol and its fluorescent derivatives induce formation of stable rescue sites in microtubules. a–c, Schemes illustrating in vitro microtubule growth events observed during control conditions and in the presence of microtubule-stabilizing drugs (MSD). Representative kymographs illustrate the dynamics of microtubules grown from GMPCPP seeds in the presence of 15 µM tubulin and 20 nM mCherry-EB3 without or with Taxol, Fchitax-3 or Flutax-2 (100 nM), as indicated. A stable rescue site in **a** is highlighted by a stippled white line. Note the enhanced green fluorescence of Fchitax-3 or Flutax-2 at the stable rescue site (white arrow). Bar graphs (mean ± s.d.) show the quantification of Fchitax-3 ($n = 65$, $N = 5$ independent experiments) and Flutax-2 ($n = 45$, $N = 3$ independent experiments) intensity on both GDP lattice and stable rescue site. The values were normalized to the intensity of the GDP lattice. Error bars represent s.d. ****$P < 0.00001$, Mann–Whitney U-test. **d**, Frequency of the occurrence (mean ± s.d.) of stable rescue sites (calculated per unit of microtubule length) at the indicated compound concentrations. ND, not detected. $n = 25$, 40 and 25 microtubules for 50, 100 and 200 nM of Fchitax-3, respectively; $n = 25$ microtubules for both Taxol and Flutax-2, three independent experiments. Error bars represent s.d. **e**, Still images, time-lapse images (corresponding to the white circle in the still image) and representative kymographs showing the formation of a dot-like Fchitax-3 accumualtion corresponding to a stable rescue site in a microtubule (MT) in a HeLa cell. Bar graph (mean ± s.d.) shows the quantification of occurrence of stable rescue sites in HeLa cells. $n = 200$ and 426 kymographs from 20 cells each for control and Fchitax-3 (100 nM)-treated sample ($N = 4$ independent experiments). Error bar represent s.d. ND, not detected.

rescues in the presence of Taxol and its fluorescent derivatives (Fig. 1a–d and Supplementary Fig. 1c–e). As described previously[21], these rescues typically happened at defined microtubule lattice sites, which we termed 'stable rescue sites' (Fig. 1a–c and Supplementary Fig. 1d). Importantly, in the case of fluorescent taxanes, we observed roughly fourfold enhanced drug binding at such sites as compared to the remainder of the microtubule lattice (Fig. 1b,c). Similar sites with increased drug accumulation inducing repeated rescues could also be detected in HeLa cells that expressed EB3-TagRFP as a microtubule plus-end marker and were incubated with 100 nM Fchitax-3 for 1 h (Fig. 1e). Comparison of the intensities of single Fchitax-3 molecules and of very short Fchitax-3 accumulations at the stable rescue sites in vitro showed that they contained ~15 molecules (Supplementary Fig. 1f–j). Taxane-induced formation of stable rescue sites thus occurs both in vitro and in cells, and ~15 drug molecules are sufficient to induce such a site.

Taxane accumulations initiate at microtubule ends

While observing microtubule growth in the presence of fluorescent taxanes, we noticed that the compounds always started to accumulate close to the growing microtubule plus- or minus-ends, directly behind the EB3-positive comet (Fig. 2a,b, Supplementary Fig. 2a and Supplementary Video 1). Taxane accumulation events appeared in a stochastic manner (Supplementary Fig. 2b) and were somewhat

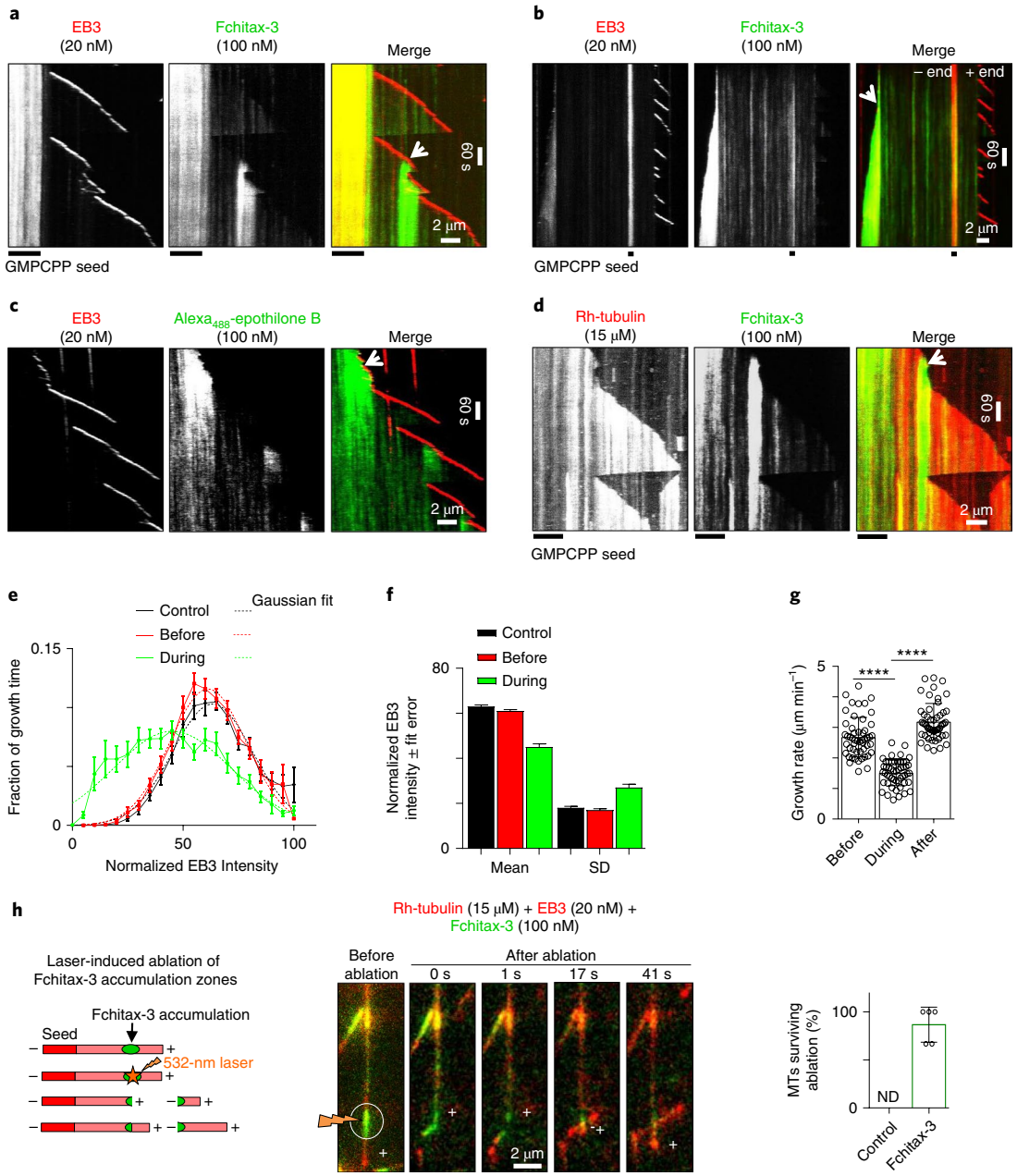

Fig. 2 | Taxane-site binding compounds accumulate at growing microtubule ends and perturb microtubule growth and depolymerization. **a–d**, Kymographs, representative of three independent experiments, illustrating the accumulation of the indicated compounds at the microtubule plus- (**a**,**c**,**d**) or minus-ends (**b**) (white arrowheads in merged panels) in the presence of 15 µM tubulin and 100 nM Fchitax-3 or $Alexa_{488}$-epothilone B, as indicated, with or without 20 nM mCherry-EB3. In **d**, 3% rhodamine-tubulin was added to the assay. **e**,**f**, Fluctuations in fluorescence intensity (mean ± s.d.) of mCherry-EB3 at microtubule tips over time in control assays (15 µM tubulin, 20 nM mCherry-EB3) or in the presence of 100 nM Fchitax-3, before or during the course of Fchitax-3 accumulation. **e**, Intensity distributions, with the experimental data denoted by solid lines and Gaussian fits by dotted lines, $n = 30$ for control and $n = 25$ for Fchitax-3-treated sample, $N = 3$ independent experiments. **f**, Plots of mean and s.d. values of the Gaussian fits. **g**, Microtubule growth rate (mean ± s.d.) in the presence of 15 µM tubulin, 20 nM mCherry-EB3 and 100 nM Fchitax-3 before, during and after Fchitax-3 accumulation. $n = 51$ in each case, $N = 3$ independent experiments, error bars represent s.d.; $^{****}P < 0.0001$ (growth rate during accumulation was compared to those before and after Fchitax-3 accumulation), Mann–Whitney *U*-test. **h**, Schematic representation and still images of laser ablation of a microtubule (MT) with a Fchitax-3 accumulation zone, observed in the presence of 15 µM tubulin (supplemented with 3% rhodamine-tubulin), 20 nM mCherry-EB3 and 100 nM Fchitax-3. The ablated microtubule region is highlighted by a lightning bolt and white circle. The positions of the plus- and minus-ends of the microtubule are indicated. Quantification (mean ± s.d.) of microtubule survival after ablation in control conditions (no drug) or within a Fchitax-3 accumulation zone ($n = 15$ microtubules from five independent experiments) is shown on the right. ND, not detected.

more prolonged and more frequent at the minus-ends (Fig. 2a,b and Supplementary Fig. 2a,c). For subsequent work, we focused on drug accumulations at the plus-ends, as minus-ends typically do not significantly elongate in vivo[27]. Consistent with the in vitro data, transient accumulations of Fchitax-3 were also observed at growing microtubule plus-ends in cells (Supplementary Fig. 2d,e).

To test whether end-dependent binding is specific for Taxol analogues, we generated an Alexa-488-labelled derivative of epothilone B (Supplementary Fig. 1a and Supplementary Fig. 3a,b), a different taxane-site binder, and found that it exhibited similar accumulations at growing microtubule ends (Fig. 2c). Drug accumulations also occurred in the absence of EB3 (Fig. 2d and Supplementary Fig. 2f); however, since EBs facilitate the detection of growing microtubule tips, subsequent experiments were carried out in the presence of EB3. During periods of strong drug accumulation, microtubule growth was perturbed, as could be seen by the reduction of EB3 signal and the microtubule growth rate (Fig. 2a,c–g). After a brief interval, an accumulation could abruptly stop and normal microtubule growth was resumed (Fig. 2a,c–g). Concomitantly, the region of enhanced drug binding persisted in the microtubule lattice (Fig. 2a,c,d). If such a growing microtubule started shrinking, microtubule depolymerization was arrested within the region with a high drug concentration, leading to rescue, which was often observed repeatedly at the same site (Fig. 2a,c and Supplementary Fig. 2a). Microtubule polymerization, with periods of perturbed growth and subsequent frequent rescues initiating within the same microtubule region, was also observed with Taxol with and without EB3 (Supplementary Fig. 2g,h). Such a behaviour is thus representative for taxane-site MTAs and is not an artefact of fluorescently labelled drugs.

To confirm that regions with high taxane accumulation have increased stability, we performed laser-severing experiments. Whereas control microtubules always depolymerized at the newly generated plus- and minus-ends (Supplementary Fig. 2i), the presence of a Fchitax-3 accumulation prevented shrinkage of freshly severed ends (Fig. 2h and Supplementary Video 2). These data demonstrate that increased taxane incorporation initiated close to a growing microtubule end leads to stabilization of a stretch of microtubule lattice.

Growth perturbations trigger taxane accumulations

Since microtubule minus-ends grow more slowly than plus-ends and show longer and more frequent Fchitax-3 accumulations (Supplementary Figs. 1c and 2c), we initially hypothesized that drugs can accumulate more easily at their luminal binding sites if microtubule polymerization is slow. However, when we varied tubulin concentration to alter the growth rate (Supplementary Fig. 4a,b), we found that Fchitax-3 accumulations became more frequent when microtubules grew more rapidly (Fig. 3a,b and Supplementary Fig. 4c). At higher growth rates, the length of Fchitax-3 accumulations increased (Fig. 3a,b and Supplementary Fig. 4c). In our assays, in the presence of EB3 without MTAs, increased tubulin concentrations led to a higher catastrophe frequency although at 25-μM tubulin we did observe some microtubules that were persistently elongating (Supplementary Fig. 4a); importantly, such microtubules still displayed frequent growth perturbations that appeared as a catastrophe followed by a rapid rescue (Supplementary Fig. 4a,b).

Interestingly, we noticed that Fchitax-3 accumulations were often initiated when microtubule polymerization appeared suboptimal or perturbed, which was often observed at microtubule minus-ends (Supplementary Figs. 1c and 2b), or when the plus-end of a GMPCPP seed had just started to elongate (Supplementary Fig. 4d). Fchitax-3 accumulation events were always accompanied by a decrease in microtubule growth rate and concomitant loss in EB3 signal (Fig. 2e–g). Analysis of the onset of such events with a higher temporal resolution, and careful alignment of the Fchitax-3 and EB3 channels, showed that on processively growing microtubules the appearance of a new Fchitax-3 accumulation occurred ~5 s after a clear reduction in EB3 signal (Fig. 3c–e). Reduction in the number of EB3-binding sites at the growing microtubule end is a hallmark of the pre-catastrophe state[28] (Supplementary Fig. 4e). Furthermore, the frequencies of catastrophes and of the appearance of Fchitax-3 accumulations at the growing microtubule ends are similar (Supplementary Fig. 4f).

We therefore wondered whether Fchitax-3 accumulations could be triggered by changes in the microtubule end conformation that lead to catastrophe. Catastrophes can potently be stimulated in our in vitro assays by different microtubule-depolymerizing agents, such as vinblastine[21], or by kinesin-13 family protein mitotic centromere-associated kinesin (MCAK)[29]. The addition of either vinblastine or GFP-MCAK, which specifically tracked growing EB3-positive microtubule ends, reduced microtubule growth rate and indeed promoted catastrophes (Supplementary Fig. 4g). These conditions are somewhat similar to the dynamics of microtubule minus-ends, which exhibit frequent growth perturbations (Supplementary Figs. 1c and 4g). Interestingly, the addition of vinblastine or GFP-MCAK increased the frequency of Fchitax-3 or $Alexa_{488}$-epothilone B accumulations, as well as the occurrence of stable rescue sites with or without EB3 (Fig. 3f–i and Supplementary Fig. 4h,i). A similar pattern of microtubule plus-end growth with frequent perturbations and repeated rescues was also observed with the combination of vinblastine and Taxol (Fig. 3j), indicating that the behaviour of fluorescent compounds is representative for taxane-site binders. It should be emphasized that vinblastine can bind to both free tubulin and the outermost microtubule tips[30], but cannot be incorporated into microtubule lattices or directly influence the conformation of the taxane-binding site within microtubule shafts. MCAK also acts at the outermost microtubule tips and is not expected to influence microtubule lattice structure[31]. Together, these data show that the perturbed structure of a microtubule end associated with the pre-catastrophe state induces the formation of lattice regions with enhanced taxane accumulation.

Analysis of Fchitax-3-binding kinetics

To understand better how Fchitax-3 accumulations are formed, we analysed their dynamics in more detail. After initiation of binding, Fchitax-3 intensity on the microtubule first rapidly increased over the course of ~50 s and then, after a period of ~100 s, it abruptly started to diminish (Fig. 4a). The rapid decline in Fchitax-3 intensity within the accumulation zone was not caused by photobleaching (Supplementary Fig. 5a, see figure legend for details), and thus was due to drug dissociation from the microtubule.

The shape of the kinetic curve, with a rapid rise and subsequent decline, suggests that some tubulin dimers first acquire an ability to bind Fchitax-3 (the initial drug accumulation phase) but later are converted to a state lacking this ability (the drug desorption phase). Because Fchitax-3 binding does not happen throughout the entire period of microtubule growth but emerges at the ends that are in a pre-catastrophe state, we defined two subsets of tubulins present at microtubule ends, which have varying ability to interact with Fchitax-3: $Tu^{receptive}$ and $Tu^{unreceptive}$. To account for desorption, we assumed that these states can be turned into the microtubule lattice-specific conformational state that does not bind to Taxol under these conditions ($Tu^{lattice}$).

To model the kinetics of Fchitax-3 accumulation and unbinding, we first used a Michaelis–Menten type of model in which Taxol was taken as a catalyst that binds $Tu^{receptive}$ (the substrate) that subsequently converts irreversibly to a non-Taxol-binding state within the microtubule lattice ($Tu^{lattice}$, the product). However, this model provided a poor fit to the experimentally obtained binding curve (Fig. 4b,c and Supplementary Fig. 5b,c). To account for the rapid and sustained increase in drug accumulation, we introduced an autocatalytic step (Fig. 4b) in which binding of Taxol to $Tu^{receptive}$ can trigger the conversion of unreceptive tubulin at microtubule ends to receptive tubulin (Fig. 4a–c and Supplementary Fig. 5d–g; see Methods for details). The obtained rate constant of Fchitax-3 binding (k_1, $5.6 \pm 0.5 \times 10^5\,M^{-1}s^{-1}$) was in good agreement with previously reported measurements for Flutax-1 and Flutax-2 (refs. [24,32]),

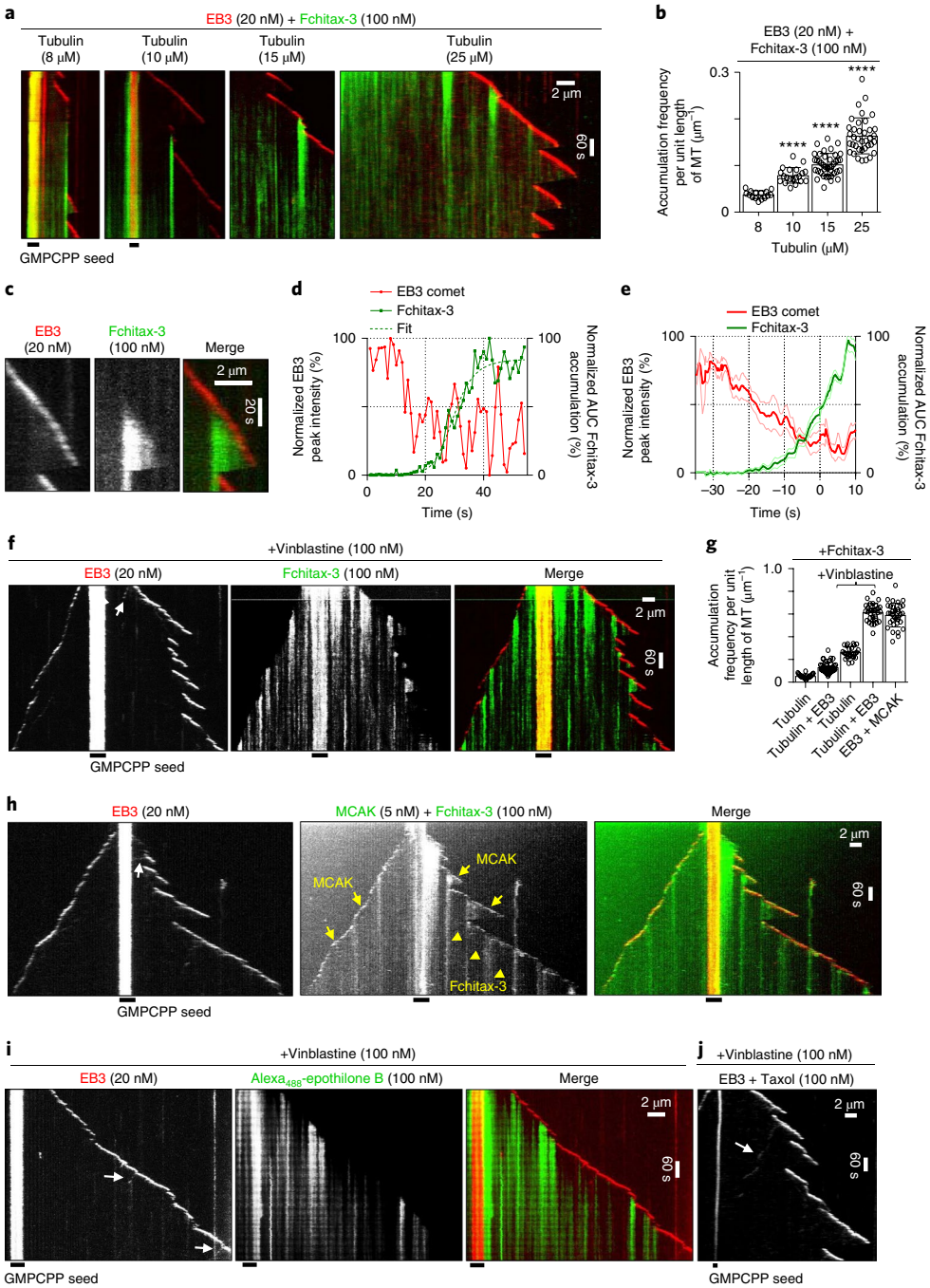

Fig. 3 | Formation of accumulations of taxane-site ligands is controlled by microtubule dynamics. a, Kymographs, representative of three independent experiments, showing Fchitax-3 accumulations in microtubules grown in the presence of the indicated tubulin concentrations, 20 nM mCherry-EB3 and 100 nM Fchitax-3. **b**, Quantification of Fchitax-3 accumulation frequency (mean ± s.d.) for the experiments shown in **a**. $n = 15$, 20, 40 and 37 accumulations in 250, 185, 135 and 94 growth events for 8, 10, 15 and 25 μM of tubulin, respectively. $N = 3$ independent experiments, error bars represent s.d., $^{****}P < 0.0001$, Mann–Whitney U-test. **c**, Kymograph showing the initiation of a Fchitax-3 accumulation associated with the reduction in mCherry-EB3 signal. $n = 5$, experimental conditions as in **a**. **d**, Time plot of the normalized maximum intensity of a fitted EB3 comet (red) and the normalized area under the curve (AUC) of a fitted Fchitax-3 (green) intensity profile. The dashed green line shows the fit of Fchitax-3 kinetics to a Hill equation (on x axis, time was used rather than concentration), representative of five experiments. **e**, Averaged EB3 and Fchitax-3 profiles (as in **d**), normalized and aligned using half-maximum effective concentration (EC_{50}) values from Hill equation fits as reference points (nine kymographs from five experiments). **f**,**h**–**j**, Kymographs (representative of three experiments) illustrating microtubule dynamics in the presence of 15 μM tubulin, 20 nM mCherry-EB3 and 100 nM vinblastine with 100 nM Fchitax-3 (**f**), or 100 nM $Alexa_{488}$-epothilone B (**i**), or 100 nM Taxol (**j**). Panel **h** shows microtubule dynamics in the presence of 15 μM tubulin, 20 nM mCherry-EB3 with 100 nM Fchitax-3 and 5 nM MCAK. Note that GFP-MCAK at growing microtubule ends and Fchitax-3 accumulations are detected in the same channel. White arrows highlight EB3 comets emerging from the accumulation zones and moving in the reverse direction. **g**, Quantification of Fchitax-3 accumulation frequencies (mean ± s.d.) per microtubule unit length in the presence of 15 μM tubulin ($n = 22$), 20 nM mCherry-EB3 ($n = 40$), 15 μM tubulin with 100 nM vinblastine ($n = 25$), 20 nM mCherry-EB3 with 100 nM vinblastine ($n = 30$) and 20 nM mCherry-EB3 with 5 nM MCAK ($n = 34$). n, number of microtubules, $N = 3$ independent experiments, error bars represent s.d.

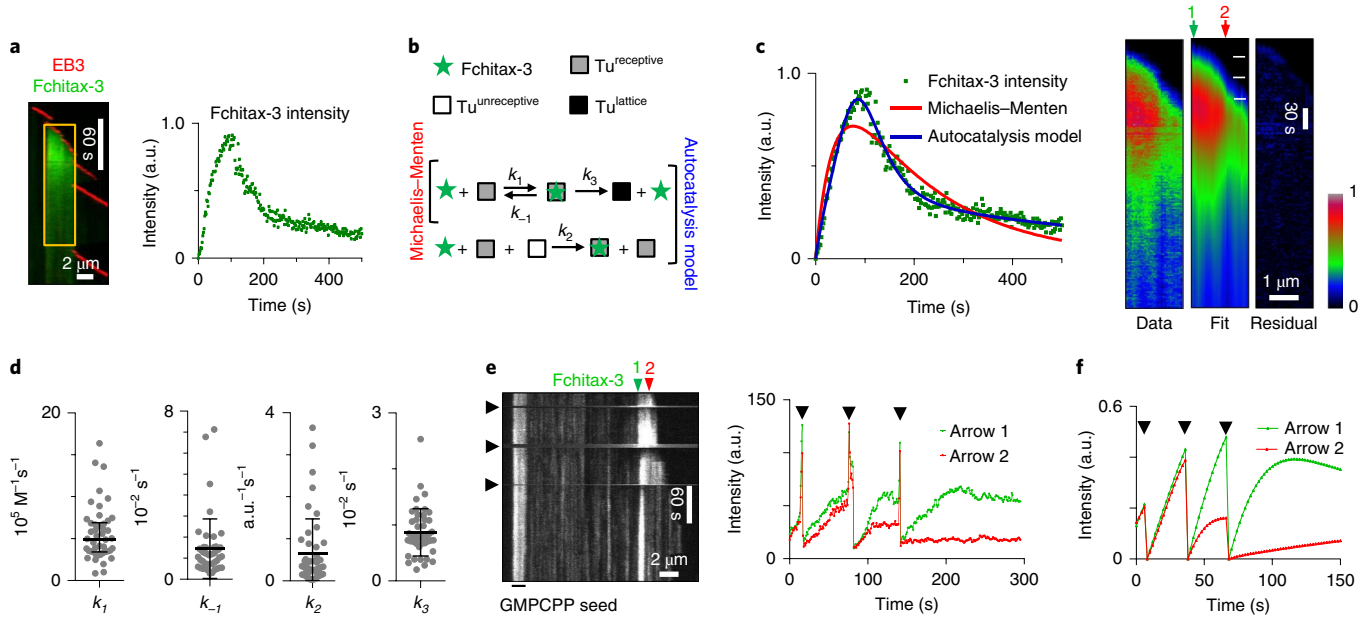

Fig. 4 | Analysis of the kinetics of Fchitax-3 accumulations. a, Kymograph, representative of five independent experiments, with a long Fchitax-3 accumulation (left) and a line intensity time trace of Fchitax-3 at the beginning of the accumulation (right). a.u., arbitrary units. **b**, Schematic kinetic diagram of the Michaelis–Menten (top reaction) and autocatalysis (top and bottom reactions) models for Fchitax-3 binding. Three tubulin states are considered: initial state unable to bind Fchitax-3 ($Tu^{unreceptive}$), Fchitax-3-binding state ($Tu^{receptive}$) and final converted state ($Tu^{lattice}$) (again, unable to bind Fchitax-3). For more details see Methods. **c**, Left: best fits to a single profile shown in **a** using either Michaelis–Menten (red line) or the autocatalysis model (blue line). Right: raw data, best fits and residuals of the autocatalysis model to the area of the kymograph bounded by a yellow rectangle in **a**. Arrows 1 and 2 indicate the positions along the microtubule for which FRAP was modelled in **f**, with white dashes indicating the moments of photobleaching used for calculation of the modelled curves. **d**, Rate constants (mean ± s.d.) of kinetic autocatalysis model (**b**) derived from intensity time trace fits (nine kymographs, 46 time traces). Error bars represent s.d. **e**, Left: kymograph of three sequential photobleaching events (highlighted by black arrowheads) of a Fchitax-3 accumulation. Right: intensity time traces along the lines marked by arrows 1 and 2 in the kymograph. Kymograph and intensity time traces are representative of three independent experiments. **f**, Modelling of FRAP curves: solutions of the model for fluorescence recovery with parameter values from fits shown in **c** (right), where the moments of photobleaching are indicated by white dashes. The same photobleaching moments are indicated by black arrowheads in **f**.

whereas the rate constant of dissociation was an order of magnitude lower (k_{-1}, $1.4 \pm 0.2 \times 10^{-2}\,s^{-1}$; Fig. 4d). This is consistent with the fact that the affinity of Fchitax-3 for its binding site is an order of magnitude higher than that of Flutax-2 (refs. [24,25]).

Next, we explored how the kinetic parameters changed along the length of the microtubule zone where an accumulation happened. In our dynamics assays, maximum Fchitax-3 intensity observed over time was typically higher at the initial point of accumulation compared to its distal end, which was formed later (Fig. 4a). In the model, this was reflected by the diminishing number of tubulin dimers per unit of microtubule length that could interact with the drug (Supplementary Fig. 5d). Furthermore, fluorescence recovery after photobleaching (FRAP) data showed that the recovery of Fchitax-3 at the starting point of an accumulation was higher compared to that at the distal end of an accumulation (Fig. 4e), and this fitted well with the modelling results (Fig. 4c,f). The higher number of drug-binding sites at the starting point of Fchitax-3 accumulation was in agreement with the observation that this region was often most resistant to depolymerization (see Fig. 3c for an example). Thus, the conformation of the microtubule zone with high taxane affinity was changing along the growing microtubule. This could have been due to certain global alterations in microtubule geometry, such as gradual closure of an open tubulin sheet. In the model, this was reflected by the variability of the autocatalysis rate constant k_2 (Fig. 4d), which can be expected to be affected by tubulin conformation in the microtubule lattice.

Quantification of the density of Fchitax-3 molecules during maximal accumulation along microtubule stretches of ~900 nm in length showed that only one or two drug molecules were bound per 8 nm, the length of one tubulin dimer (Supplementary Fig. 5h). Since GMPCPP-nucleated microtubules in our assays are expected to have ~14 protofilaments, this means that even at the highest binding density the microtubule is still far from being saturated with the drug. It should be noted that, since this quantification is based on the average fluorescence intensity, it is possible that Fchitax-3 molecules are distributed in an irregular fashion—for example, with neighbouring tubulin subunits being preferentially in either bound or unbound state. Combined with the modelling, our data suggest that taxanes display cooperative binding to microtubules even at low saturation, implying that changes in drug-binding affinity can propagate in microtubule lattices.

Nucleotide state of tubulin affects Fchitax-3 binding

Since growing microtubule ends maintain a GTP cap that is gradually hydrolysed, and because tubulin undergoes nucleotide-dependent conformational changes[10,16,33], enhanced Fchitax-3 binding at growing microtubule tips could be due to a particular nucleotide state. Fchitax-3 and other tested taxanes indeed showed preference for GMPCPP seeds and GMPCPP-containing microtubule extensions as compared to guanosine-5'-diphosphate (GDP)-bound lattices (Fig. 5a,b). FRAP analysis of Fchitax-3 signal on GMPCPP seeds provided an estimate for the dissociation constant (k_{-1} FRAP, $2.2 \pm 0.3 \times 10^{-2}\ s^{-1}$), which was similar to the values derived from our autocatalysis kinetic model (Fig. 5c,d). In contrast, Fchitax-3 had no preference for guanosine 5'-O-[gamma-thio]triphosphate (GTPγS)-bound microtubules, which are thought to mimic the

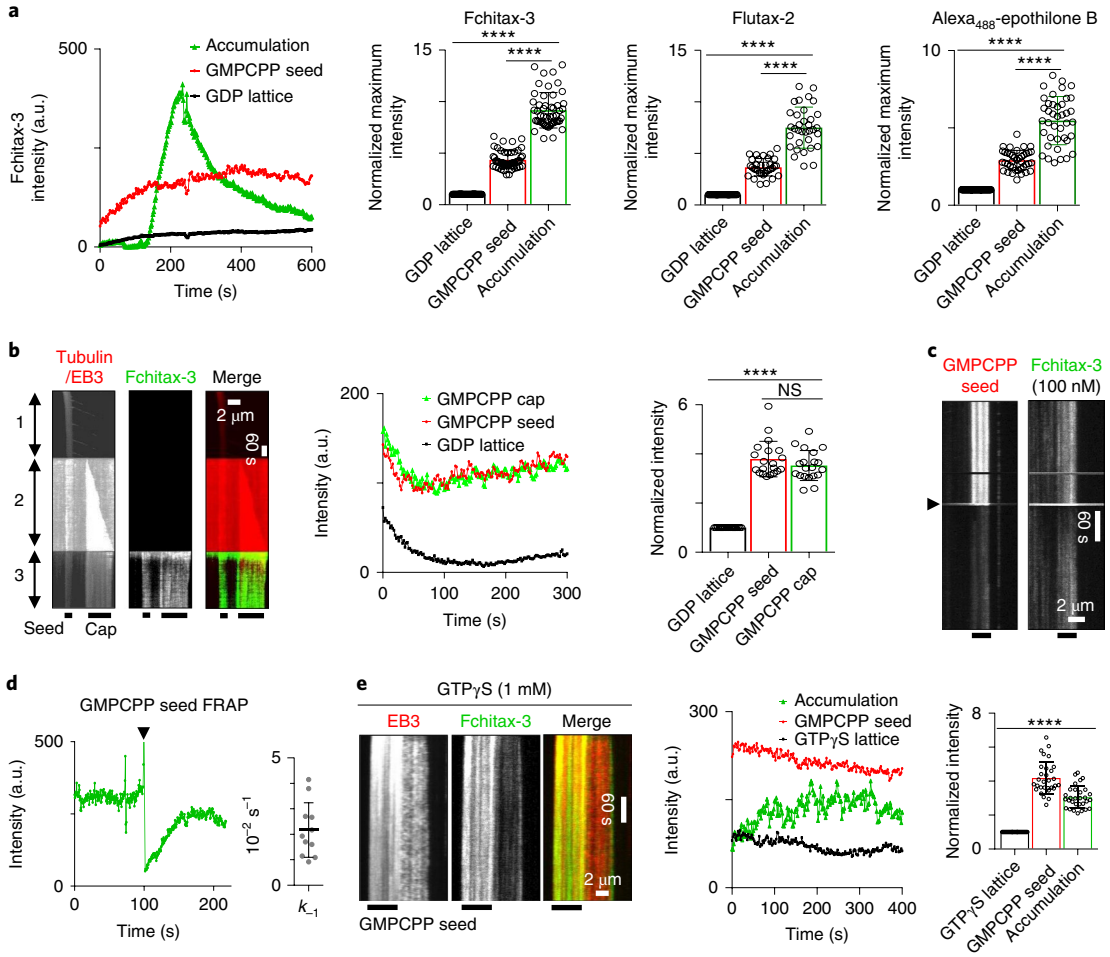

Fig. 5 | Analysis of the nucleotide dependence of Fchitax-3 accumulations. a, Fchitax-3 (100 nM) fluorescence intensity profile on GMPCPP-stabilized microtubule seed, dynamic microtubule lattice (GDP lattice) and within a Fchitax-3 accumulation. Bar graphs (mean values) show quantification of the normalized maximum value of fluorescence intensity on GMPCPP-stabilized microtubule seed, GDP lattice and within a Fchitax-3 ($n=50$, $N=5$), Flutax-2 ($n=34$, $N=3$) or Alexa$_{488}$-epothilone B ($n=40$, $N=3$) accumulation zone. The values were normalized to the intensity of the GDP lattice. Error bars represent s.d. ****$P<0.0001$, Mann–Whitney U-test. **b**, Kymographs illustrating in vitro dynamics of a microtubule that was first grown from a GMPCPP seed in the presence of 15 µM tubulin and 20 nM mCherry-EB3 (1), in the presence of 5 µM tubulin supplemented with 3% rhodamine-tubulin and 250 µM GMPCPP (GMPCPP cap) (2) and then incubated with 100 nM Fchitax-3 (3). Fluorescence intensity profiles and Fchitax-3 intensities (mean) normalized to the intensity of the GDP lattice are shown on the right. $n=20$, $N=3$ independent experiments. Error bars represent s.d., ****$P<0.0001$; NS, not significant, $P=0.25$, Mann–Whitney U-test. **c**,**d**, Representative kymographs, single-line intensity time traces and plot (mean value) showing the rate constant of photobleaching of Fchitax-3 within GMPCPP seeds. $n=11$, $N=5$ independent experiments. Error bar represents s.d. Black arrowhead indicates the time point when photobleaching was performed. **e**, Representative kymographs, intensity profiles and a plot (mean) showing quantification of the intensity of Fchitax-3 fluorescence for GMPCPP-stabilized seed, microtubule lattice grown in the presence of 15 µM tubulin, 20 nM mCherry-EB3, 1 mM GTPγS and 100 nM Fchitax-3 (GTPγS lattice) and the Fchitax-3 accumulation zone within the same microtubule. Intensity values were normalized to the intensity of the GTPγS lattice. $n=30$ from $N=3$ independent experiments, error bars represent s.d., ****$P<0.0001$, Mann–Whitney U-test.

GTP hydrolysis intermediate GDP-inorgainc phosphate (GDP-Pi) state of tubulin[11,33] (Fig. 5e).

Preferential binding to GMPCPP microtubules might be due to their longitudinally extended lattice conformation, because Taxol was reported to induce similar microtubule lattice extension when added during, though not after, microtubule assembly[11,16,33,34]. To gain support for the idea that Taxol affects tubulin dimer length within microtubules, we performed X-ray fibre diffraction experiments with microtubules that were assembled from GTP-tubulin and were either untreated or treated with Taxol during or after polymerization (Supplementary Fig. 6a–e). Both Taxol-treated samples exhibited increased dimer length compared to drug-free microtubules, though this length was slightly shorter in samples treated with Taxol after assembly (Supplementary Fig. 6f,g). Similarly, microtubules assembled from GDP-tubulin incubated with Taxol during polymerization also displayed extended lattice (Supplementary Fig. 6d–g) (note that GDP-tubulin does not polymerize without Taxol and, therefore, the effect of Taxol could not be tested under post-assembly conditions). Taxol can thus induce changes in microtubule lattice compaction that could contribute to the observed binding preferences and cooperativity. However, the maximum intensity of Fchitax-3 accumulations at microtubule ends greatly exceeded the intensity of the drug binding to GMPCPP-stabilized seeds present in the same microtubules (Fig. 5a). Furthermore, Fchitax-3 accumulations could also form at microtubule tips in the presence of GTPγS, although in this case their intensity was typically lower than that at GMPCPP-containing microtubule seeds in the same assay (Fig. 5e). We therefore conclude that the nucleotide state of tubulin

and the associated changes in the longitudinal lattice compaction can affect taxane binding, but that they are not sufficient to explain the strong drug accumulations at microtubule ends. In particular, rapid release of Fchitax-3 from the accumulation zones and the abrupt transitions between regions of high and low drug binding can best be explained by additional global conformational transitions, such as the closure of a microtubule sheet into a tube.

Taxanes induce tube closure defects

To investigate whether the presence of taxane accumulations is indeed associated with deviations in microtubule structure, we performed cryo-EM analysis of GMPCPP-stabilized microtubule seeds, control microtubules, microtubules grown in the presence of either Fchitax-3 or vinblastine, or both agents together (Fig. 6a–d and Supplementary Fig. 7a–c). GMPCPP-stabilized microtubule seeds showed a regular geometry with very few, small defects ($\lesssim$40 nm) (Supplementary Fig. 7a). Whereas Fchitax-3 had no effect on the abundance of small microtubule defects ($\lesssim$40 nm), we observed in its presence a significant increase in the frequency of incomplete microtubule shaft regions >40 nm (Fig. 6a–d). Very long regions of incomplete microtubule lattices were seen when Fchitax-3 and vinblastine were combined (Supplementary Fig. 7b,c). These data strongly suggest that the regions of enhanced Fchitax-3 binding represent microtubule regions that failed to close into a complete microtubule tube.

Incomplete microtubule lattice structures are expected to show increased flexibility, and we indeed observed a strong increase in transverse microtubule tip fluctuations during the formation of Fchitax-3 accumulations (Fig. 6e). It should be noted that Taxol binding can, per se, reduce microtubule rigidity[34–36] and it is possible that this effect contributes to the flexible character of the Fchitax-3 accumulation zones.

To confirm that Fchitax-3-grown microtubules contain interrupted protofilaments, we used as a tool the microtubule minus-end-binding protein CAMSAP3. CAMSAPs recognize free microtubule minus-ends because their signature domain, CKK, binds in a minus-end-specific manner to interprotofilament sites at uncapped microtubule extremities[37]. Interestingly, distinct CAMSAP3 binding was observed at ~30% of Fchitax-3 accumulations (Fig. 6f and Supplementary Fig. 7d). Over time, the CAMSAP3 signal extended in the minus-end direction (Fig. 6f). Since CAMSAPs decorate growing microtubule minus-ends[38], these data indicate that Fchitax-3 accumulations can create regions of incomplete microtubule lattice that can be extended by tubulin addition. These data also explain why Fchitax-3 accumulation zones can serve as the origin of EB3-positive comets (Fig. 3f,h, white arrows in EB3 panels), which highlight growing protofilament plus- and minus-ends. Similar events were also observed in the presence of Taxol (Fig. 3i, white arrows).

Next, we used FRAP assays in the tubulin channel to test for tubulin incorporation at the Fchitax-3 accumulation zones. Whereas control microtubule lattices showed no fluorescence recovery (Supplementary Fig. 7e), Fchitax-3 accumulation zones displayed clear recovery of the tubulin signal (Fig. 6g). In some cases, the length of tubulin incorporation detected after photobleaching was up to ~1 µm (Supplementary Fig. 7f). We also frequently observed transient binding of EB3, a marker of growing microtubule ends, within the drug accumulation areas (Fig. 6h and Supplementary Fig. 7g). These data indicate that tubulin indeed incorporates into microtubule lattice within Fchitax-3 accumulation zones. Such microtubule repair explains why the length of microtubule lattice defects observed by electron microscopy (~100 nm) was much shorter than that of Fchitax-3 accumulation zones, which could extend to several micrometres (compare Fig. 6d and Supplementary Fig. 7h). These results indicate that the formation of Fchitax-3 accumulations is associated with major microtubule lattice defects, such as missing parts of protofilaments that are partly restored by tubulin incorporation.

Discussion

In this study, we found that the association of taxane-site ligands with microtubules preferentially occurs at growing microtubule ends and is strongly dependent on the conformational state of these ends, leading to a highly uneven binding pattern along the microtubule shaft. This observation helps to explain why taxane-site ligands have a stronger effect on microtubule lattice structure when added during, and not after, microtubule polymerization[34,39]. Previous models of Taxol stabilization mechanisms assumed a stochastic but homogeneous change in the rate constants and thermodynamic states of tubulin dimers within a microtubule[40]. In contrast our data show that, at non-saturating concentrations of the compound, microtubule stabilization is achieved by the formation of specific zones (local 'clusters') with an increased stability, possibly due to a cooperative change in the microtubule lattice structure. The formation

Fig. 6 | Fchitax-3 promotes long, sheet-like microtubule defects and generates sites of tubulin incorporation. a,**b**, Cryo-EM images (representative of two experiments) of microtubules grown with 15 µM tubulin and 20 nM mCherry-EB3 without (**a**) or with (**b**) 100 nM Fchitax-3. Long, sheet-like defects are boxed. **c**,**d**, Quantification of percentage of total defects (**c**) and defects of certain length (**d**) in GMPCPP-stabilized, control (–Fchitax-3) ($n = 311$ microtubules) and Fchitax-3-treated microtubules (+Fchitax-3) ($n = 833$ microtubules), combined from two experiments each. $^{****}P < 0.0001$; NS, no statistically significant difference, $P = 0.2$, Pearson's χ^2 test. **e**, Top: time-lapse images illustrating that Fchitax-3 accumulation is accompanied by microtubule bending. Bottom left: an example of transverse microtubule tip fluctuations. Bottom right: average standard deviation (normalized to the values before Fchitax-3 accumulation) of the microtubule tip fluctuations before, during and after Fchitax-3 accumulation. $n = 11$, $N = 5$, $^{**}P = 0.0038$; NS, no statistically significant difference, $P = 0.55$, Mann–Whitney U-test. **f**, Left: kymographs illustrating microtubule dynamics with 15 µM tubulin, 20 nM GFP-EB3, 100 nM Fchitax-3 and 10 nM mCherry-CAMSAP3. Middle: scheme illustrating CAMSAP3 binding to a microtubule minus-end and protofilaments extending from a Fchitax-3 accumulation in the minus-end direction. Right: fluorescence intensity profiles and quantifications (mean ± s.d.) showing CAMSAP3 intensity at the microtubule regions grown from the minus- (1) and plus-end (2) of the seed and Fchitax-3 accumulation (3). Data were normalized to the CAMSAP3 intensity of the microtubule grown from the minus-end (2). $n = 10$, $N = 3$ independent experiments. **g**, Left: kymographs showing FRAP within microtubule region with Fchitax-3 accumulation. White lightning bolt highlights the bleached region, and white arrowheads highlight tubulin fluorescence recovery within bleached area. Middle: fluorescence intensity profiles of unbleached and bleached microtubule regions with and without Fchitax-3 accumulation. Right: quantification (mean ± s.d.) of tubulin fluorescence before, during and after photobleaching in control microtubules ($n = 14$) and microtubule regions with a Fchitax-3 accumulation ($n = 15$), $N = 3$ independent experiments. $^{****}P < 0.0001$, $^{*}P = 0.1$, Mann–Whitney U-test. **h**, Quantification (mean ± s.d.) of EB3 fluorescence at growing plus-ends or within microtubule regions with or without Fchitax-3 accumulation ($n = 30$ microtubules from $N = 3$ independent experiments). Intensity values were normalized to the intensity of EB3 at growing microtubule plus-ends.$^{****}P < 0.0001$, Mann–Whitney U-test. **i**, Model showing interaction of taxane-site ligands with microtubules. Taxanes show preference for GMPCPP- over GDP-bound microtubule lattice. The onset of catastrophe promotes taxane binding, possibly due to end tapering and the appearance of tubulin sheets. The drugs exhibit binding cooperativity and stabilize these microtubule structures. Subsequently, the regular microtubule structure is re-established due to tubulin incorporation; however, remnants of an incomplete microtubule structure with a high drug affinity remain; they stabilize the site, incorporate GTP-tubulin and promote repeated rescues.

of local clusters is reminiscent of polymorphic transitions in crystals, suggesting that the addition of a taxane-site ligand to dynamic microtubules induces altered forms of microtubule lattices.

The nucleotide state of tubulin plays a role in controlling taxane affinity for microtubules, with the GMPCPP-bound, extended conformation being preferred over the compacted GDP or GTPγS lattice, consistent with the data that both GMPCPP- and Taxol-bound microtubules have expanded lattice[10,33,34]. However, the pattern of ligand binding to a growing microtubule cannot be explained by the nucleotide state of tubulin alone. Our data

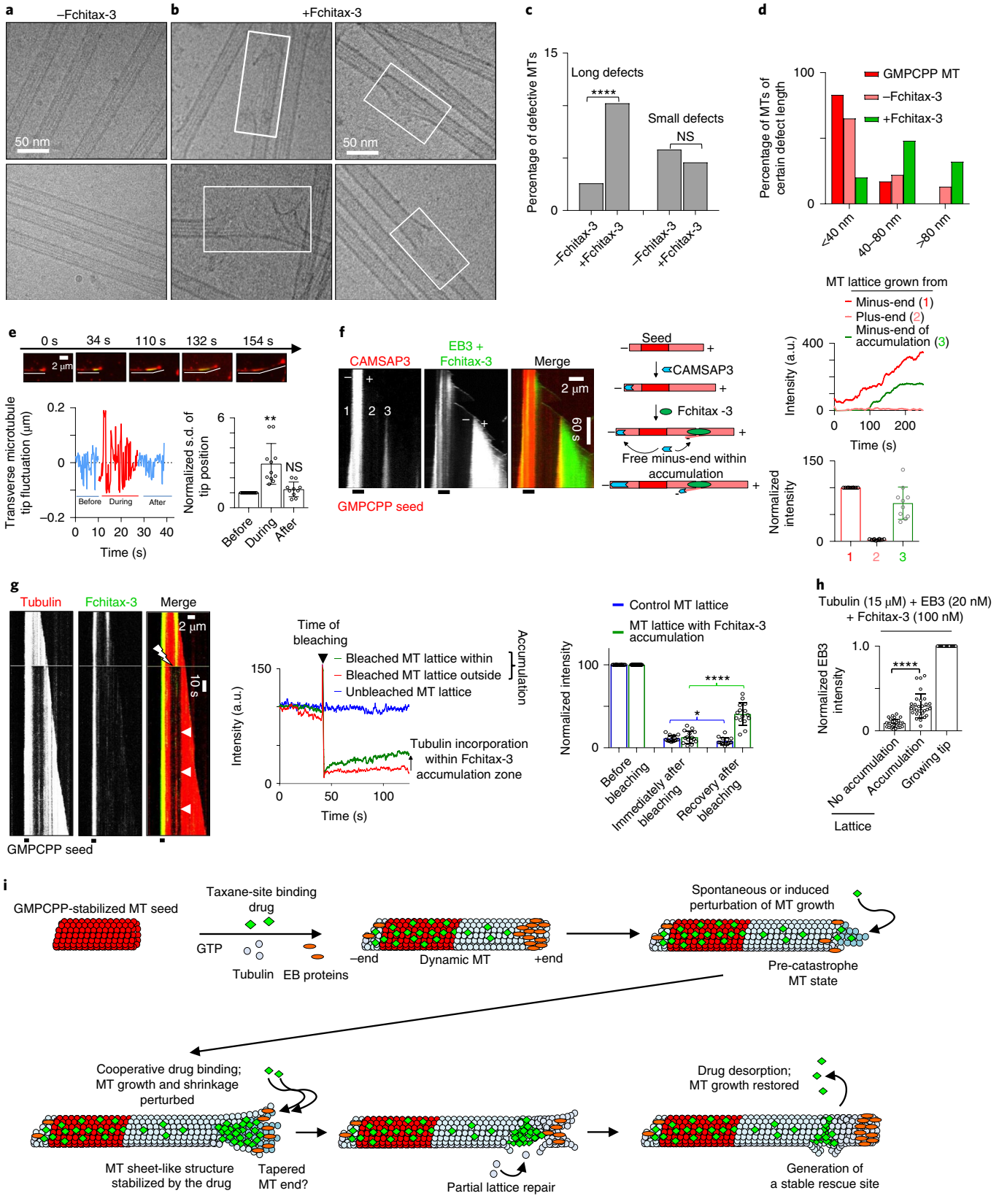

suggest that taxane-site ligands can preferentially bind to incomplete microtubule structures present at the ends, and strongly modify the properties, of these structures (Fig. 6i). The increased affinity of taxanes for incomplete tubulin structures, such as tubulin sheets, can explain their binding kinetics: providing the tube is incomplete, taxane keeps binding, but if the sheet closes into a tube, a significant proportion of the drug molecules is released. Our data are consistent with the idea that, after tube closure and growth continuation, an open structure remains at the initial part of the drug accumulation zone, explaining why the drug can still exchange within this region and create a stable site that inhibits microtubule depolymerization. Incorporation of GTP-tubulin at the drug accumulation zones promotes their stability and their capacity to induce rescues, as described previously for other situations where microtubule lattice repair has been observed[41–43]. Importantly, our data suggest that microtubule repair at drug accumulation sites is not complete—a part of the microtubule lattice remains open, but is not depolymerized due to the presence of drug molecules.

An interesting feature of taxane binding to microtubule lattices is its cooperative character. Our modelling based on the kinetic binding curves suggests that initially only a few tubulin dimers within the microtubule lattice can bind the drug, and that drug association catalyses the formation of additional binding sites in the vicinity. One potential explanation of such cooperativity could be based on the propagation of an extended conformational state of the microtubule lattice, which was observed for Taxol-bound microtubules by cryo-EM[10,33,34] and in our X-ray fibre diffraction experiments. A similar elongation of the axial microtubule repeat has recently been proposed to underlie the positive cooperativity in the binding of kinesin-1 to microtubules[44]. However, since taxane-site ligands can also affect lateral contacts between tubulin dimers[13–16], it is possible that alterations in these contacts account for propagating structural effects, such as a differential curvature of tubulin sheets.

Taxane-bound zones at microtubule ends represent suboptimal substrates for microtubule shrinkage, but also for microtubule growth. This leads to slow growth and frequent transitions between growth and shortening, which helps to explain the surprising observation that, although Taxol is a microtubule stabilizer, at low concentrations it perturbs microtubule growth in cells (reviewed in ref. [45]; see ref. [22] for an example).

An important conclusion of our study is that the conformational transitions at microtubule ends, which lead to growth perturbation and catastrophes, also promote taxane-site ligand binding and microtubule stabilization by these compounds. One interesting consequence of this effect is that the distribution of ligand accumulations along the microtubule shaft reflects the history of the growth of this microtubule. Another important consequence is that taxane-site ligand binding to microtubules can be potentiated by low doses of catastrophe-inducing MTAs, and some evidence supporting this idea has already been reported based on cell culture experiments[23]. Our data provide an explanation for this phenomenon and suggest that, in future work, it can be exploited for optimization of MTA-based cancer therapies.

Online content

Any methods, additional references, Nature Research reporting summaries, source data, extended data, supplementary information, acknowledgements, peer review information; details of author contributions and competing interests; and statements of data and code availability are available at https://doi.org/10.1038/s41563-019-0546-6.

Received: 2 February 2019; Accepted: 24 October 2019;
Published online: 9 December 2019

References

1. Desai, A. & Mitchison, T. J. Microtubule polymerization dynamics. *Annu. Rev. Cell Dev. Biol.* **13**, 83–117 (1997).
2. Cross, R. A. Microtubule lattice plasticity. *Curr. Opin. Cell Biol.* **56**, 88–93 (2018).
3. Kueh, H. Y. & Mitchison, T. J. Structural plasticity in actin and tubulin polymer dynamics. *Science* **325**, 960–963 (2009).
4. Brouhard, G. J. & Rice, L. M. Microtubule dynamics: an interplay of biochemistry and mechanics. *Nat. Rev. Mol. Cell Biol.* **19**, 451–463 (2018).
5. Dumontet, C. & Jordan, M. A. Microtubule-binding agents: a dynamic field of cancer therapeutics. *Nat. Rev. Drug Discov.* **9**, 790–803 (2010).
6. Yang, C. H. & Horwitz, S. B. Taxol((R)): the first microtubule stabilizing agent. *Int. J. Mol. Sci.* **18**, E1733 (2017).
7. Steinmetz, M. O. & Prota, A. E. Microtubule-targeting agents: strategies to hijack the cytoskeleton. *Trends Cell Biol.* **28**, 776–792 (2018).
8. Nogales, E. & Kellogg, E. H. Challenges and opportunities in the high-resolution cryo-EM visualization of microtubules and their binding partners. *Curr. Opin. Struct. Biol.* **46**, 65–70 (2017).
9. Elie-Caille, C. et al. Straight GDP-tubulin protofilaments form in the presence of taxol. *Curr. Biol.* **17**, 1765–1770 (2007).
10. Alushin, G. M. et al. High-resolution microtubule structures reveal the structural transitions in alphabeta-tubulin upon GTP hydrolysis. *Cell* **157**, 1117–1129 (2014).
11. Zhang, R., Alushin, G. M., Brown, A. & Nogales, E. Mechanistic origin of microtubule dynamic instability and its modulation by EB proteins. *Cell* **162**, 849–859 (2015).
12. Kellogg, E. H. et al. Near-atomic model of microtubule–tau interactions. *Science* **360**, 1242–1246 (2018).
13. Prota, A. E. et al. Molecular mechanism of action of microtubule-stabilizing anticancer agents. *Science* **339**, 587–590 (2013).
14. Prota, A. E. et al. Structural basis of microtubule stabilization by discodermolide. *Chembiochem* **18**, 905–909 (2017).
15. Wang, Y. et al. Mechanism of microtubule stabilization by taccalonolide AJ. *Nat. Commun.* **8**, 15787 (2017).
16. Manka, S. W. & Moores, C. A. The role of tubulin-tubulin lattice contacts in the mechanism of microtubule dynamic instability. *Nat. Struct. Mol. Biol.* **25**, 607–615 (2018).
17. Brown, T. et al. A phase I trial of taxol given by a 6-hour intravenous infusion. *J. Clin. Oncol.* **9**, 1261–1267 (1991).
18. Weaver, B. A. How Taxol/paclitaxel kills cancer cells. *Mol. Biol. Cell* **25**, 2677–2681 (2014).
19. Gianni, L. et al. Nonlinear pharmacokinetics and metabolism of paclitaxel and its pharmacokinetic/pharmacodynamic relationships in humans. *J. Clin. Oncol.* **13**, 180–190 (1995).
20. Spratlin, J. & Sawyer, M. B. Pharmacogenetics of paclitaxel metabolism. *Crit. Rev. Oncol. Hematol.* **61**, 222–229 (2007).
21. Mohan, R. et al. End-binding proteins sensitize microtubules to the action of microtubule-targeting agents. *Proc. Natl Acad. Sci. USA* **110**, 8900–8905 (2013).
22. Bouchet, B. P. et al. Mesenchymal cell invasion requires cooperative regulation of persistent microtubule growth by SLAIN2 and CLASP1. *Dev. Cell* **39**, 708–723 (2016).
23. Photiou, A., Shah, P., Leong, L. K., Moss, J. & Retsas, S. In vitro synergy of paclitaxel (Taxol) and vinorelbine (navelbine) against human melanoma cell lines. *Eur. J. Cancer* **33**, 463–470 (1997).
24. Diaz, J. F., Strobe, R., Engelborghs, Y., Souto, A. A. & Andreu, J. M. Molecular recognition of Taxol by microtubules. Kinetics and thermodynamics of binding of fluorescent taxol derivatives to an exposed site. *J. Biol. Chem.* **275**, 26265–26276 (2000).
25. Li, X., Barasoain, I., Matesanz, R., Diaz, J. F. & Fang, W. S. Synthesis and biological activities of high affinity taxane-based fluorescent probes. *Bioorg. Med. Chem. Lett.* **19**, 751–754 (2009).
26. Bieling, P. et al. Reconstitution of a microtubule plus-end tracking system in vitro. *Nature* **450**, 1100–1105 (2007).
27. Akhmanova, A. & Steinmetz, M. O. Control of microtubule organization and dynamics: two ends in the limelight. *Nat. Rev. Mol. Cell Biol.* **16**, 711–726 (2015).
28. Duellberg, C., Cade, N. I., Holmes, D. & Surrey, T. The size of the EB cap determines instantaneous microtubule stability. *eLife* **5**, e13470 (2016).
29. Montenegro Gouveia, S. et al. In vitro reconstitution of the functional interplay between MCAK and EB3 at microtubule plus ends. *Curr. Biol.* **20**, 1717–1722 (2010).
30. Gigant, B. et al. Structural basis for the regulation of tubulin by vinblastine. *Nature* **435**, 519–522 (2005).
31. Friel, C. T. & Welburn, J. P. Parts list for a microtubule depolymerising kinesin. *Biochem. Soc. Trans.* **46**, 1665–1672 (2018).
32. Diaz, J. F., Barasoain, I. & Andreu, J. M. Fast kinetics of Taxol binding to microtubules. Effects of solution variables and microtubule-associated proteins. *J. Biol. Chem.* **278**, 8407–8419 (2003).

33. Zhang, R., LaFrance, B. & Nogales, E. Separating the effects of nucleotide and EB binding on microtubule structure. *Proc. Natl Acad. Sci. USA* **115**, E6191–E6200 (2018).
34. Kellogg, E. H. et al. Insights into the distinct mechanisms of action of taxane and non-taxane microtubule stabilizers from cryo-EM structures. *J. Mol. Biol.* **429**, 633–646 (2017).
35. Mitra, A. & Sept, D. Taxol allosterically alters the dynamics of the tubulin dimer and increases the flexibility of microtubules. *Biophys. J.* **95**, 3252–3258 (2008).
36. Kikumoto, M., Kurachi, M., Tosa, V. & Tashiro, H. Flexural rigidity of individual microtubules measured by a buckling force with optical traps. *Biophys. J.* **90**, 1687–1696 (2006).
37. Atherton, J. et al. A structural model for microtubule minus-end recognition and protection by CAMSAP proteins. *Nat. Struct. Mol. Biol.* **24**, 931–943 (2017).
38. Jiang, K. et al. Microtubule minus-end stabilization by polymerization-driven CAMSAP deposition. *Dev. Cell* **28**, 295–309 (2014).
39. Arnal, I. & Wade, R. H. How does Taxol stabilize microtubules? *Curr. Biol.* **5**, 900–908 (1995).
40. Castle, B. T. et al. Mechanisms of kinetic stabilization by the drugs paclitaxel and vinblastine. *Mol. Biol. Cell* **28**, 1238–1257 (2017).
41. Schaedel, L. et al. Microtubules self-repair in response to mechanical stress. *Nat. Mater.* **14**, 1156–1163 (2015).
42. Aumeier, C. et al. Self-repair promotes microtubule rescue. *Nat. Cell Biol.* **18**, 1054–1064 (2016).
43. Vemu, A. et al. Severing enzymes amplify microtubule arrays through lattice GTP-tubulin incorporation. *Science* **361**, eaau1504 (2018).
44. Shima, T. et al. Kinesin-binding-triggered conformation switching of microtubules contributes to polarized transport. *J. Cell Biol.* **217**, 4164–4183 (2018).
45. Jordan, M. A. & Wilson, L. Microtubules as a target for anticancer drugs. *Nat. Rev. Cancer* **4**, 253–265 (2004).

Methods

Reagents and purified proteins. Taxol was purchased from Enzo Life Sciences. Vinblastine sulfate, GTP, glucose oxidase from *Aspergillus niger*, catalase from bovine liver, methylcellulose, dithiothreitol (DTT), 1,4-piperazinediethanesulfonic acid (PIPES), piperazine-1,4-bis(2-ethanesulfonic acid), piperazine-N,N′-bis(2-ethanesulfonic acid), magnesium chloride, ethylene glycol-bis(2-aminoethylether)-N,N,N′,N′-tetraacetic acid (EGTA), potassium hydroxide, potassium chloride, κ-casein, glucose, fetal bovine serum and penicillin-streptomycin antibiotic were obtained from Sigma-Aldrich. GMPCPP was obtained from Jena Biosciences. Biotinylated poly(L-lysine)-[g]-poly(ethylene glycol) (PLL-PEG-biotin) was obtained from Susos AG. NeutrAvidin was acquired from Invitrogen. DMEM and F10 media and LT07-518 Mycoalert assay were obtained from Lonza. Trypsin-EDTA was from acquired Biowest. FuGENE 6 was supplied by Roche. Different types of labelled and unlabelled purified tubulin used in the assays were either obtained from Cytoskeleton or purified as described previously[46] for fibre diffraction experiments. mCherry-CAMSAP3 and GFP-MCAK were purified as described previously[38,47].

Synthesis of Alexa$_{488}$-epothilone B. Alexa$_{488}$-epothilone B was prepared by click reaction between an alkyne group-containing, C-6-modified epothilone B analogue and an azide-containing derivative of Alexa-488. Alexa Fluor 488 Azide (2.18 mg, 2.53 µmol, 1.00 eq) and C-6-modified epothilone B analogue GS-240 (1.45 mg, 2.53 µmol, 1.00 eq) were suspended in a mixture of tert-butyl alcohol and water (1/1, 0.20 ml). To this suspension Tris[(1-benzyl-1H-1,2,3-triazol-4-yl)methyl] amin (0.40 mg, 0.758 µmol, 0.30 eq) was added, and freshly prepared aqueous sodium ascorbate solution (1 M solution in water, 2.5 µl, 2.53 µmol, 1.00 eq), followed by an aqueous copper sulfate pentahydrate solution (0.8 M, 0.6 µl, 0.505 µmol, 0.2 eq). The reaction mixture was stirred for 4 h at room temperature until high-performance liquid chromatography (HPLC) control showed complete conversion. The solvents were then removed under reduced pressure, and the resulting residue was dissolved in a mixture of MeCN and water (1/2, 0.4 ml) until a clear solution had formed. This solution was then directly purified by preparative HPLC (SymmetryPrep C18, 5 µm, 19 × 100 mm^2; MeCN/water 0/100 to MeCN/water 100/0 over 15 min, retention time 9.1 min). Lyophilization gave the compound Alexa$_{488}$-epothilone B as a pink solid (2.71 mg, 2.20 µmol, 87%).

In vitro assay for microtubule dynamics. In vitro assay for microtubule growth dynamics was performed as described previously[29]. Briefly, as described previously[48], GMPCPP-stabilized microtubule seeds were prepared by two cycles of microtubule polymerization and depolymerization in the presence of GMPCPP (a slowly hydrolysable GTP analogue). A solution of porcine brain tubulin (20 µM) mix containing biotin-labelled tubulin (18%) and rhodamine-labelled tubulin (12%) was polymerized in MRB80 buffer (80 mM K-PIPES, pH 6.8, 4 mM $MgCl_2$, 1 mM EGTA) in the presence of GMPCPP (1 mM) at 37 °C for 30 min. After polymerization, the mixture was pelleted by centrifugation in an Airfuge for 5 min at 119,000*g*. The pellet thus obtained was resuspended in MRB80 buffer, depolymerized on ice for 20 min and further polymerized in the presence of GMPCPP. After the second round of polymerization and pelleting, GMPCPP-stabilized microtubule seeds were stored in MRB80 containing 10% glycerol. In vitro flow chambers for TIRF microscopy were assembled on microscopic slides by two strips of double-sided tape with plasma-cleaned glass coverslips. Flow chambers were sequentially incubated with 0.2 mg ml^{-1} PLL-PEG-biotin and 1 mg ml^{-1} NeutrAvidin in MRB80 buffer. Flow chambers were further incubated with GMPCPP-stabilized microtubule seeds followed by treatment with 1 mg ml^{-1} κ-casein. The reaction mixtures (15 µM porcine brain tubulin supplemented with 3% rhodamine-tubulin when indicated, 20 nM mCherry-EB3 or GFP-EB3 when indicated, 50 mM KCl, 1 mM guanosine triphosphate, 0.1% methylcellulose, 0.2 mg ml^{-1} κ-casein and oxygen scavenger mixture (50 mM glucose, 400 µg ml^{-1} glucose oxidase, 200 µg ml^{-1} catalase and 4 mM DTT in MRB80 buffer)), with or without MTAs, GFP-MCAK or mCherry-CAMSAP3, were added to the flow chambers after centrifugation in an Airfuge for 5 min at 119,000*g*. Flow chambers were sealed with vacuum grease, and microtubule dynamics was recorded using TIRF microscopy. During in vitro sample imaging, all samples were maintained at 30 °C and cells were imaged at 37 °C.

Cell culture. HeLa and HEK293T cells, obtained from the American Type Culture Collection (ATCC), were cultured in DMEM/Ham's F10 media (1/1 ratio) supplemented with 10% fetal calf serum and 1% antibiotics (penicillin and streptomycin). ATCC performs short-tandem repeat profiling for cell line authentication, and no additional cell line authentication was performed. The cell line used here was not found in the database of commonly misidentified cell lines maintained by the Immunization Coalition of Los Angeles County. The cell line was routinely checked for mycoplasma contamination using LT07-518 Mycoalert assay. To determine the cellular effects of Fchitax-3, HeLa cells, transiently transfected with EB3-TagRFP[21,47] using FuGENEF 6, were treated with 100 nM Fchitax-3 for 1 h. Cell imaging was performed using TIRF microscopy.

Image acquisition by TIRF microscopy and image analysis. Imaging was performed on a TIRF microscope set-up (inverted research microscope, Nikon Eclipse Ti-E), which was equipped with the perfect focus system (Nikon) and a Nikon CFI Apo TIRF ×100/1.49 numerical aperture oil objective (Nikon). The microscope was supplemented with a TIRF-E motorized TIRF illuminator, modified by Roper Scientific/PICT-IBiSA Institut Curie, and a stage-top incubator (model no. INUBG2E-ZILCS, Tokai Hit) was used to regulate the temperature of the sample. Image acquisition was performed using either a Photometrics Evolve 512 EMCCD camera (Roper Scientific) or a Photometrics CoolSNAP HQ2 CCD camera (Roper Scientific), and controlled with MetaMorph 7.7 software (Molecular Devices). For simultaneous imaging of red and green fluorescence, we used triple-band TIRF polychroic ZT405/488/561rpc (Chroma) and a triple-band laser emission filter (no. ZET405/488/561 m, Chroma), mounted in the metal cube (Chroma, no. 91032), together with an Optosplit III beamsplitter (Cairn Research) equipped with a double-emission filter cube configured with ET525/50 m, ET630/75 m and T585LPXR (Chroma). Measurement of 491-nm laser power under TIRF conditions was performed using a ThorLabs optical power and energy metre (PM400) unit with S170C sensor. Under TIRF conditions, maximum laser intensity (100% laser power) for a 491-nm laser was found to be 160 µW.

ImageJ plugin KymoResliceWide v.0.4 (https://github.com/ekatrukha/KymoResliceWide) was used to generate kymographs to represent the life history of microtubule dynamics. As described previously[21,29], microtubule dynamics parameters from kymographs were determined with an optimized version of the custom-made JAVA plugin for ImageJ. For catastrophe frequency quantification, short depolymerization events (as depicted in Supplementary Fig. 4a, white arrow) were also considered a catastrophe event.

Single-molecule intensity analysis . To estimate the fluorescence intensity of single molecules of Fchitax-3, two parallel flow chambers were made on the same coverslip. In one chamber, regular microtubule dynamic assay in the presence of GMPCPP-stabilized microtubule seeds with tubulin, mCherry-EB3 and Fchitax-3 was performed. The other chamber was incubated with the same concentration of Fchitax-3 but without the reaction mixture. In both conditions, the first 10–20 images of unexposed coverslip areas were acquired at 100-ms exposure time using low laser intensity, and then a video of 10–20 frames exposing the same area with continuous laser illumination was recorded to induce photobleaching of Fchitax-3 molecules. Fluorescence intensities of Fchitax-3 molecules binding to the coverslip in both chambers were detected and measured using ImageJ plugin DoM_Utrecht v.0.9.1 (https://github.com/ekatrukha/DoM_Utrecht). The fitted peak intensity values were used to build fluorescence intensity histograms, which were compared to the intensity of Fchitax-3 signal on microtubules. The histograms were fitted to Gaussian distributions using GraphPad Prism 7.

Analysis of EB3 intensity fluctuations at the microtubule plus-end. The distributions of EB3 intensities (normalized to the maximum value) were analysed during the course of a growth event under control conditions (15 µM tubulin, 20 nM EB3) or with the addition of 100 nM Fchitax-3. In the case of Fchitax-3, fluctuations in EB3 intensity were analysed before, and during the course of, the initiation of Fchitax-3 accumulation. For control measurements, we excluded the EB3 signal during the final phase of growth before catastrophe (pre-catastrophe phase) from our analysis, because at this point the comet intensity is reduced[21,49].

Laser ablation of microtubules in vitro. Laser photoablation assay, in which an individual microtubule is severed by a focused laser beam, was performed on the TIRF microscope equipped with an ILas system (Roper Scientific/PICT-IBiSA) and a 532-nm Q-switched pulsed laser (Teem Photonics). In vitro microtubule dynamics assay was performed in the presence of GMPCPP-stabilized microtubule seeds with 15 µM tubulin, supplemented with 3% rhodamine-tubulin and 20 nM mCherry-EB3 with or without 100 nM Fchitax-3.

Fluorescence recovery after photobleaching (FRAP) assay. FRAP assay, in which a region of a microtubule is bleached by a focused laser beam, was carried out on the TIRF microscope equipped with an ILas system (Roper Scientific/PICT-IBiSA). In vitro microtubule dynamics assay was performed in the presence of GMPCPP-stabilized microtubule seeds with 15 µM tubulin, supplemented with 3% rhodamine-tubulin without (control) or with 100 nM Fchitax-3. Photobleaching in the tubulin channel was performed with the 561-nm laser. In the case of control, a segment of GDP microtubule lattice was photobleached. In the case of Fchitax-3-containing samples, photobleaching was performed in the microtubule segment with the Fchitax-3 accumulation zone.

X-ray fibre diffraction experiments. X-ray fibre diffraction images were collected in beamline BL11-NCD-SWEET of ALBA Synchrotron. Purified bovine tubulin was diluted to a final concentration of 100 µM of PEM buffer (80 mM PIPES, 1 mM EGTA, 0.2 mM Tris, 1 mM DTT, 3 mM $MgCl_2$). GDP-tubulin was obtained from diluted tubulin by hydrolysis, through incubation of diluted protein for 30 min at 37 °C and then supplementing the samples with 1 mM GDP. GTP-tubulin was obtained by supplementing the dilution buffer with 2 mM GTP. Microtubules were obtained by incubating tubulin samples for 30 min at 37 °C to achieve maximum polymerization. For Taxol-treated samples, 200 µM Taxol was added to the samples either before microtubule polymerization (pre-assembly assays)

or after polymerization (post-assembly assays). The samples were then mixed at 1/1 volume ratio with pre-warmed PEM buffer containing 2% methylcellulose (MO512, Sigma-Aldrich). Final concentrations of protein, nucleotide and compounds were 50 µM tubulin, 100 µM Taxol and 1 mM GTP or 1 mM GDP. Samples were centrifuged for 10 s at 2,000*g* to eliminate air bubbles, and transferred to a share-flow device[50,51].

For each condition, a total of 24 diffraction images were averaged and background subtracted using ImageJ software (v.1.51j8, Wayne Rasband, National Institutes of Health, Bethesda, MD, USA). Angular image integrations were performed using XRTools software (obtained from beamline BM26-DUBBLE of the European Synchrotron Radiation Facility). For average monomer length determination, the fourth harmonic of the first layer of line signals (1-nm peak, fourth layer line) was fitted to a single-peaked Lorentzian function using SigmaPlot software (v.12.0) using peak maxima distance to centre to calculate average monomer length.

Averaging of EB3 and Fchitax-3 intensity time traces. Simultaneous two-colour imaging of Fchitax-3/mCherry-EB3 was performed using an OptoSplit III beamsplitter (Cairn Research) equipped with a double-emission filter cube projecting two channels on the camera chip simultaneously. Cromatic aberrations were corrected as described previously, using calibration photomask[47]. Registered videos were used to create kymographs by drawing segmented lines of width ten pixels (0.65 µm) along growing microtubules using KymoResliceWide plugin with maximum transverse intensity (http://fiji.sc/KymoResliceWide). On extracted kymographs, we outlined a rectangular region of interest around observed accumulation events and exported both intensities. For each frame, we fitted the mCherry-EB3 profile with the sum of constant (lattice binding) and exponential decay functions (comet) convoluted with the microscope's point spread function:

$$I(x,t) = I_{BG} + \tfrac{1}{2} I_{lattice} \times \mathrm{erfc}\left(\tfrac{x-x_c}{\sqrt{2}\sigma}\right) + \\ + \tfrac{1}{2} I_{peak} \times \exp\left(\tfrac{\lambda}{2}(\sigma^2\lambda + 2(x-x_c))\right) \times \left(1 - \mathrm{erf}\left(\tfrac{\sigma^2\lambda + x - x_c}{\sqrt{2}\sigma}\right)\right) \quad (1)$$

where fitting parameter I_{BG} corresponds to the intensity of background, $I_{lattice}$, to the amplitude of the fluorescent intensity fraction associated with the lattice binding, I_{peak}, to the amplitude of convolved exponential decay, x_c to the position of the maximum number of molecules in the molecules distribution (start of exponential decay position), σ to the point spread function standard deviation and λ to the exponential decay constant. erf is an error function and erfc is complementary error function. From the fitted function $I(x,t)$ at each time frame, t, we obtained maximum fluorescent intensity $I_{EB3}(t) = \max_x I(x,t)$.

The intensity of Fchitax-3 was fitted with Gaussian function with background, where the width was a fitting parameter. Total intensity was calculated as an integrated area under the fitted curve (without background intensity) and provided $I_{Fchitax3}(t)$. This function for each kymograph was further fitted with a dose–response Hill equation, substituting the concentration for time:

$$I_{Fchitax3}(t) = I_{BG} + \frac{I_{Max} - I_{BG}}{1 + \left(\frac{\tau_{50\%}}{t}\right)^h} \quad (2)$$

where I_{Max} is maximum intensity of Fchitax-3, h is a Hill coefficient and $\tau_{50\%}$ corresponds to the time when intensity reaches half of its value. The choice of Hill equation was simply a matter of convenience—other sigmoid-like functions (for example, error function) worked equally well. All $I_{EB3}(t)$ and $I_{Fchitax3}(t)$ intensity traces were normalized by the minimum and maximum values and shifted in such a way that $\tau_{50\%}$ moments were aligned (making this point $t=0$). For averaging of same-time sampling moments, intensity profiles were linearly interpolated with steps of 0.1 per frame.

Analysis of microtubule fluctuations. To estimate the transversal fluctuations of the microtubule tip before, during and after Fchitax-3 accumulation, we first determined the position of the microtubule tip. Tracking of microtubule plus-ends was performed using Trackmate plugin in Fiji (http://fiji.sc/TrackMate)[52]. Post-processing of the tracks was carried out by a custom-made script in MATLAB. For each growth event, the tracking provided coordinates $x(t_i)$ and $y(t_i)$ of the fluorescent peak of an EB3 comet in the plane of the coverslip over time points $t_i, i \in [1,\ldots,N]$. The trajectory of the comet was fit with a straight line, $y = mx + c$ (forced to pass through x_S and y_S) to find the average axis of microtubule growth. To split the movement of the microtubule end into longitudinal $x_r(t)$ and transverse $y_r(t)$ components, we moved the origin of coordinates to the plus-end of the microtubule seed and rotated the x–y plane to align the microtubule growth axis with the x axis using the transform:

$$\begin{bmatrix} x_r \\ y_r \end{bmatrix} = \begin{bmatrix} \cos\theta & -\sin\theta \\ \sin\theta & \cos\theta \end{bmatrix} \begin{bmatrix} x - x_S \\ y - y_S \end{bmatrix} \quad (3)$$

where the value of rotation angle θ is equal to $\arctan(m)$. The characteristic s.d. of the transverse deflection was calculated as

$$\sigma_y = \sqrt{\frac{1}{N-1}\sum_{i=1}^{N}(y_r(t_i) - \overline{y_r})} \quad (4)$$

where y_r is the average deflection per track.

Cryo-EM. For sample preparation, microtubules were polymerized from GMPCPP seeds with 1 mM GTP, 15 µM Tubulin, 20 nM mCherry-EB3 and in the absence or presence of 100 nM Fchitax-3 at 37 °C for 10 min (designated –Fchitax-3 and +Fchitax-3 sample, respectively). Four microlitres of each sample was applied to holey carbon grids (C-flat 2/2, Protochips) and glow-discharged in air before blotting and plunge-freezing using Vitrobot Mark IV (Thermo Fisher Scientific) at 22 °C and 100% humidity.

All cryo-EM micrographs were collected using a Tecnai T12 transmission electron microscope (Thermo Fisher) with a 4×4 K CCD camera (Gatan) at 120 kV, magnification ×52,000, image pixel size 2.09 Å and defocus around –5 µm.

For microtubule defect analysis, images from the –Fchitax-3 and +Fchitax-3 datasets collected by one team member were randomly mixed and were scored blindly by another team member for the presence/absence of small lattice defects (≲40 nm) and larger, sheet-like lattice defects (≳40 nm). Only microtubules that were longer than half a frame width and were not squashed by adjacent microtubules were included in the analysis. Following scoring, the frequency data were regrouped according to polymerization condition, and differences between ±Fchitax-3 microtubules were evaluated for statistical significance using Pearson's χ^2 test in GraphPad Prism 7.

Statistical analysis. All the histograms were plotted in GraphPad Prism 7, and statistical analysis was done using non-parametric Mann–Whitney *U*-tests. For Fig. 6c, a one-sided Pearson's χ^2 test was performed. All reported experiments were performed two or more times independently.

Kinetic model of Fchitax-3 accumulation. To understand how the observed dynamics of Fchitax-3 accumulation can emerge from the underlying molecular interactions, we generated a set of kinetic models based on our imaging data. Comparison of models to experimental data allowed us to eliminate contradictory mechanisms and narrow down the set to a single model, presented in Fig. 4b. Below, we describe the considered models and their underlying assumptions.

Initially, Fchitax-3 does not bind to microtubule lattice continuously and its accumulation occurs only at specific moments during microtubule growth. Therefore we assumed that, at some time point, a special tubulin state ($Tu^{receptive}$) becomes accessible at the tip of a growing microtubule. This tubulin state can bind Fchitax-3 molecules, leading to the formation of a ($Tu^{receptive}$–Fchitax-3) complex, as observed in experiments. Since after the initial accumulation the intensity of Fchitax-3 at microtubules irreversibly declines (Fig. 4a), we postulated that there is a transition from the Fchitax-3-bound tubulin state to another state ($Tu^{lattice}$) that is unable to bind Fchitax-3 (accompanied by release of Fchitax-3). This transition can be attributed to the overall structural rearrangement of microtubule lattice. The described kinetic scheme is equivalent to the Michaelis–Menten model[53] (denoted here as M1), where tubulin is considered as a substrate and Fchitax-3 as an enzyme. Assuming that Fchitax-3 concentration in solution remains constant, the corresponding kinetic equations are:

$$\frac{dx(t)}{dt} = -k_1[\mathrm{Fchitax3}]x + k_{-1}y \quad (M1.1)$$

$$\frac{dy(t)}{dt} = k_1[\mathrm{Fchitax3}]x - k_{-1}y - k_3 y \quad (M1.2)$$

$$x(0) = [Tu^{receptive}]_0,\ y(0) = 0; \\ x(t) = [Tu^{receptive}](t),\ y(t) = [Tu^{receptive} \times \mathrm{Fchitax3}](t) \quad (M1.3)$$

where $x(t)$ corresponds to the concentration of ($Tu^{receptive}$) tubulin state, $y(t)$ to its complex with Fchitax-3 ($Tu^{receptive}$–Fchitax3), k_1 and k_{-1} are the rate constants of Fchitax-3 binding and unbinding, respectively, and k_3 is the rate constant of transition to ($Tu^{lattice}$) state. We assumed that, at the initial moment, there is no ($Tu^{receptive}$–Fchitax3) complex present and that there is some fixed number of ($Tu^{receptive}$) binding sites.

To fit model (M1.1–1.3) to experimental data, we built a kymograph of accumulation using KymoResliceWide plugin v.0.5 for Fiji (https://github.com/ekatrukha/KymoResliceWide) using the 'maximum intensity transverse to line' option. We subtracted background intensity from the kymograph of Fchitax-3 and normalized it by maximum intensity value (after background subtraction). In this way, the maximum number of Fchitax-3 molecules per pixel over the whole duration of accumulation is equal to one. We built Fchitax-3 intensity traces over time at each pixel position along microtubule zones with Fchitax-3 accumulation. To estimate the initial moment of accumulation at specific positions along the microtubule, we fitted the initial phase of increasing Fchitax-3 intensity with a dose–response Hill equation, substituting the concentration for time:

$$I_{\mathrm{Fchitax3}}(t) = I_{\mathrm{BG}} + \frac{I_{\mathrm{Max}} - I_{\mathrm{BG}}}{1 + \left(\frac{\tau_{50\%}}{t}\right)^{h}} \quad (5)$$

The choice of the Hill equation was simply a matter of convenience—other sigmoid-like functions (for example, error function) worked equally well. The fitting was performed in MATLAB. We estimated the initial moment of accumulation as $\tau_{3\%}$:

$$\tau_{3\%} = \tau_{50\%}\left(\frac{3\%}{100\% - 3\%}\right)^{1/h} \quad (6)$$

Choosing any other value between 1 or 3% did not change the outcome of the analysis. At each pixel of accumulation along a microtubule, the normalized Fchitax-3 intensity from the moment of $\tau_{3\%}$ until the end of the acquisition was used as an input to fit a kinetic model. Analytical solution of the model (M1.1–3) was found using Mathematica v.11.0.1.0 (Wolfram Research). The derived function, $y(t)$—that is, the solution of M1.2 and M1.3—was fitted to the Fchitax-3 intensity time trace with NonlinearModelFit function using rate constants and initial concentration values as fitting parameters.

The final best fit of the Michaelis–Menten model (see Fig. 4c for a representative example) did not provide a satisfactory description of the shape of the kinetic curve. This discrepancy can be attributed to the fact that simple binding–unbinding kinetics (M1.1) cannot produce the observed rapid increase in the accumulation of Fchitax-3, and required the addition of a nonlinearity. To overcome this, we introduced a simple autocatalysis/cooperativity step, where the presence of the ($\mathrm{Tu}^{\mathrm{receptive}}$–Fchitax3) complex increases the probability of Fchitax-3 binding to ($\mathrm{Tu}^{\mathrm{receptive}}$) tubulin (see Supplementary Fig. 5b). The modified kinetic equations are:

$$\frac{\mathrm{d}x(t)}{\mathrm{d}t} = -k_1[\mathrm{Fchitax3}]x + k_{-1}y - k_2xy \quad (M2.1)$$

$$\frac{\mathrm{d}y(t)}{\mathrm{d}t} = k_1[\mathrm{Fchitax3}]x - k_{-1}y + k_2xy - k_3y \quad (M2.2)$$

$$x(0) = \left[\mathrm{Tu}^{\mathrm{receptive}}\right]_0,\ y(0) = 0;\quad x(t) = \left[\mathrm{Tu}^{\mathrm{receptive}}\right](t),\ y(t) = \left[\mathrm{Tu}^{\mathrm{receptive}} \times \mathrm{Fchitax3}\right](t) \quad (M2.3)$$

where k_2 corresponds to the rate constant of the autocatalysis. Since this system of differential equations (M2.1–2.3) cannot be solved analytically, it was solved numerically using the ParametricNDSolveValue function of Mathematica. The same function and workflow were also used for the other nonlinear models described below in this section. Residuals between the solution and experimental data were minimized using NonlinearModelFit function with a Levenberg–Marquardt optimizer. Due to physical constrains on parameter values (that is, rate constant values should be always positive), the optimizer did not always converge to a true minimum in the parameter space, sometimes stalling at the borders. In this case, the relative fitting errors of parameters exceeded 100%. For such fits, another set of initial parameters for the optimizer was chosen. If the minimum was still not found, the fit was discarded.

Model 2 (M2) provided a much better fit to the experimentally observed kinetic curve (Supplementary Fig. 5c,e), confirming that the addition of an autocatalysis step is necessary to explain the experimental data. However, this model yielded values of the dissociation constant, k_{-1}, in the range 0.2–0.5 s^{-1}, one order of magnitude higher than those estimated from FRAP experiments (Fig. 5d). Simulated FRAP experiments show that Fchitax-3 recovery is almost immediate, contradicting experimental data (Fig. 4e and Supplementary Fig. 5f). This can be explained by the fact that the dissociation rate in this case has to compensate for the much faster Fchitax-3 association, which is self-accelerated due to autocatalysis. Therefore, we excluded this kinetic mechanism.

In both models described above, it was assumed that a Fchitax-3 accumulation starts with the sudden appearance of a substantial amount of ($\mathrm{Tu}^{\mathrm{receptive}}$) tubulin state (GMPCPP-like) at the tip of the growing microtubule (Supplementary Fig. 5e). Instantaneous emergence of such a structure seemed implausible. Therefore, we considered an alternative scenario where the majority of tubulin molecules exist in some initial state ($\mathrm{Tu}^{\mathrm{unreceptive}}$) that is unable to bind Fchitax-3. If a small number of ($\mathrm{Tu}^{\mathrm{receptive}}$) tubulins appears, this leads to ($\mathrm{Tu}^{\mathrm{receptive}}$–Fchitax3) complex formation that can catalyse the transition of additional ($\mathrm{Tu}^{\mathrm{unreceptive}}$) tubulin molecules to the ($\mathrm{Tu}^{\mathrm{receptive}}$) state. The corresponding kinetic equations are:

$$\frac{\mathrm{d}x(t)}{\mathrm{d}t} = -k_1[\mathrm{Fchitax3}]x + k_{-1}y \quad (M3.1)$$

$$\frac{\mathrm{d}y(t)}{\mathrm{d}t} = k_1[\mathrm{Fchitax3}]x - k_{-1}y + k_2zy - k_3y \quad (M3.2)$$

$$\frac{\mathrm{d}z(t)}{\mathrm{d}t} = -k_2zy \quad (M3.3)$$

$$x(0) = \left[\mathrm{Tu}^{\mathrm{receptive}}\right]_0;\ y(0) = 0;\ z(0) = \left[\mathrm{Tu}^{\mathrm{unreceptive}}\right]_0,\quad x(t) = \left[\mathrm{Tu}^{\mathrm{receptive}}\right](t),\ y(t) = \left[\mathrm{Tu}^{\mathrm{receptive}} \times \mathrm{Fchitax3}\right](t),\ z(t) = \left[\mathrm{Tu}^{\mathrm{unreceptive}}\right](t) \quad (M3.4)$$

where $z(t)$ corresponds to the concentration of ($\mathrm{Tu}^{\mathrm{unreceptive}}$) tubulin state and k_2 is the rate constant of autocatalysis. The numerical solution of the (M3.1–3.4) model is highly unstable, but nevertheless the best obtained fits provided a poor description of experimental data (Supplementary Fig. 5c). In addition, the values of dissociation constant k_{-1} were in the same range as in model (M2.1–2.3), contradicting our FRAP data.

After considering different kinetic schemes we found that a model where the binding of Fchitax-3 to ($\mathrm{Tu}^{\mathrm{receptive}}$), per se, catalyses the transformation of another (possibly neighbouring) ($\mathrm{Tu}^{\mathrm{unreceptive}}$) to ($\mathrm{Tu}^{\mathrm{receptive}}$) state best describes experimental data. The corresponding system of kinetic equations is:

$$\frac{\mathrm{d}x(t)}{\mathrm{d}t} = -k_1[\mathrm{Fchitax3}]x + k_{-1}y \quad (M4.1)$$

$$\frac{\mathrm{d}y(t)}{\mathrm{d}t} = k_1[\mathrm{Fchitax3}]x - k_{-1}y + k_2zx - k_3y \quad (M4.2)$$

$$\frac{\mathrm{d}z(t)}{\mathrm{d}t} = -k_2zx \quad (M4.3)$$

$$x(0) = \left[\mathrm{Tu}^{\mathrm{receptive}}\right]_0;\ y(0) = 0;\ z(0) = \left[\mathrm{Tu}^{\mathrm{unreceptive}}\right]_0,\quad x(t) = \left[\mathrm{Tu}^{\mathrm{receptive}}\right](t),\ y(t) = \left[\mathrm{Tu}^{\mathrm{receptive}} \times \mathrm{Fchitax3}\right](t),\ z(t) = \left[\mathrm{Tu}^{\mathrm{unreceptive}}\right](t) \quad (M4.4)$$

The final best fits of the model (M4.1–4.4), together with FRAP simulations, are presented in Fig. 4c,f. Solutions for the kinetics of ($\mathrm{Tu}^{\mathrm{unreceptive}}$), ($\mathrm{Tu}^{\mathrm{receptive}}$) and ($\mathrm{Tu}^{\mathrm{receptive}}$–Fchitax-3) for a representative fit are shown in Supplementary Fig. 5g. To calculate the kinetics of FRAP, we first solved equations (M4.1–4.4) until the moment of bleaching, t_{FRAP}. After that, we considered the following system:

$$\frac{\mathrm{d}\tilde{x}(t)}{\mathrm{d}t} = -k_1[\mathrm{Fchitax3}]\tilde{x} + k_{-1}\tilde{y} + k_{-1}y_{\mathrm{bleached}} \quad (M4F.1)$$

$$\frac{\mathrm{d}\tilde{y}(t)}{\mathrm{d}t} = k_1[\mathrm{Fchitax3}]\tilde{x} - k_{-1}\tilde{y} + k_2\tilde{z}\tilde{x} - k_3\tilde{y} \quad (M4F.2)$$

$$\frac{\mathrm{d}\tilde{z}(t)}{\mathrm{d}t} = -k_2\tilde{z}\tilde{x} \quad (M4F.3)$$

$$\frac{\mathrm{d}y_{\mathrm{bleached}}(t)}{\mathrm{d}t} = -k_{-1}y_{\mathrm{bleached}} - k_3y_{\mathrm{bleached}} \quad (M4F.4)$$

$$\tilde{x}(0) = x(t_{FRAP});\ y_{\mathrm{bleached}}(0) = y(t_{\mathrm{FRAP}});\ \tilde{z}(0) = z(t_{\mathrm{FRAP}});\ \tilde{y}(0) = 0 \quad (M4F.5)$$

where $y_{\mathrm{bleached}}(t)$ corresponds to the concentration of the photobleached molecules of the ($\mathrm{Tu}^{\mathrm{receptive}}$–Fchitax3) complex after time t_{FRAP}, and $\tilde{y}(t)$ are the newly absorbed molecules.

For the long accumulation event presented in Fig. 4a, we explored the dependence of model parameters on the position along an accumulation. Rate constants k_1, k_{-1} and k_3 fluctuated slightly around their average values and did not show any significant trends. In contrast, the initial concentrations of ($\mathrm{Tu}^{\mathrm{unreceptive}}$) and ($\mathrm{Tu}^{\mathrm{unreceptive}}$) monotonically declined from their position at the beginning of accumulation towards its end (Supplementary Fig. 5d). This means that the size of structure on the microtubule lattice that interacts with Fchitax-3 is gradually decreasing, which might be attributed to the structural 'closure' of microtubule lattice.

Reporting Summary. Further information on research design is available in the Nature Research Reporting Summary linked to this article.

Data availability

All data that support the conclusions are available from the authors on request, and/or also available in the Supplementary Information.

Code availability

All MATLAB and Mathematica notebooks used for computations, together with the raw data, are available online at https://doi.org/10.6084/m9.figshare.7520033 and https://github.com/RuddiRodriguez/Analysis-of-MT-plus-end-fluctuations.

References

46. Diaz, J. F. & Andreu, J. M. Assembly of purified GDP-tubulin into microtubules induced by Taxol and Taxotere: reversibility, ligand stoichiometry, and competition. *Biochemistry* **32**, 2747–2755 (1993).
47. Aher, A. et al. CLASP suppresses microtubule catastrophes through a single TOG domain. *Dev. Cell* **46**, 40–58 e48 (2018).
48. Gell, C. et al. Microtubule dynamics reconstituted in vitro and imaged by single-molecule fluorescence microscopy. *Methods Cell Biol.* **95**, 221–245 (2010).
49. Maurer, S. P., Fourniol, F. J., Bohner, G., Moores, C. A. & Surrey, T. EBs recognize a nucleotide-dependent structural cap at growing microtubule ends. *Cell* **149**, 371–382 (2012).
50. Sugiyama, T. et al. Quick shear-flow alignment of biological filaments for X-ray fiber diffraction facilitated by methylcellulose. *Biophys. J.* **97**, 3132–3138 (2009).
51. Kamimura, S., Fujita, Y., Wada, Y., Yagi, T. & Iwamoto, H. X-ray fiber diffraction analysis shows dynamic changes in axial tubulin repeats in native microtubules depending on paclitaxel content, temperature and GTP-hydrolysis. *Cytoskeleton (Hoboken)* **73**, 131–144 (2016).
52. Tinevez, J. Y. et al. TrackMate: an open and extensible platform for single-particle tracking. *Methods* **115**, 80–90 (2017).
53. Michaelis, L., Menten, M. L., Johnson, K. A. & Goody, R. S. The original Michaelis constant: translation of the 1913 Michaelis–Menten paper. *Biochemistry* **50**, 8264–8269 (2011).

Acknowledgements

We thank G. Fernando Díaz for calf brain supply, and the staff of beamline BL11-NCD-SWEET (ALBA) for their support with the X-ray fibre diffraction experiments. We thank S. Kamimura (Chuo University) for kindly providing the share-flow device employed for fibre diffraction experiments. This work was supported by the European Research Council Synergy (grant no. 609822) and the Netherlands Organization for Scientific Research CW ECHO (grant no. 711.015.005 to A.A.), by a Biotechnology and Biological Sciences Research Council grant (no. BB/N018176/1 to C.A.M.), by an EMBO Long Term Fellowship to R.R.-G., by the CAMS Innovation Fund for Medical Sciences (grant no. 2016-I2M-1-010 to W.-S.F.), by grants from MINECO/FEDER (no. BFU2016-75319-R to J.F.D.) and by COST Action (no. CM1407 to J.F.D. and K.-H.A.). M.O.S is supported by a grant from the Swiss National Science Foundation (no. 31003A_166608).

Author contributions

A.R. designed and performed experiments, analysed data and wrote the paper. T.L. and C.A.M. designed and performed cryo-EM experiments and analysed data. E.A.K. analysed data and performed the modelling. J.E.-G. performed X-ray fibre diffraction experiments. R.R.-G. analysed microtubule tip fluctuation data. W.-S.F. synthesized Fchitax-3 and Flutax-2. S.G. and K.-H.A. synthesized Alexa$_{488}$-epothilone B. L.C.K., J.F.D. and M.O.S. contributed to the design of the experiments and analysis of the data and models. A.A. designed experiments, coordinated the project and wrote the paper.

Competing interests

The authors declare no competing interests.

Additional information

Supplementary information is available for this paper at https://doi.org/10.1038/s41563-019-0546-6.

Correspondence and requests for materials should be addressed to A.A.

Reprints and permissions information is available at www.nature.com/reprints.

nature research

Corresponding author(s): Akhmanova

Last updated by author(s): Sep 20, 2019

Reporting Summary

Nature Research wishes to improve the reproducibility of the work that we publish. This form provides structure for consistency and transparency in reporting. For further information on Nature Research policies, see Authors & Referees and the Editorial Policy Checklist.

Statistics

For all statistical analyses, confirm that the following items are present in the figure legend, table legend, main text, or Methods section.

n/a	Confirmed
☐	☒ The exact sample size (*n*) for each experimental group/condition, given as a discrete number and unit of measurement
☐	☒ A statement on whether measurements were taken from distinct samples or whether the same sample was measured repeatedly
☐	☒ The statistical test(s) used AND whether they are one- or two-sided *Only common tests should be described solely by name; describe more complex techniques in the Methods section.*
☒	☐ A description of all covariates tested
☒	☐ A description of any assumptions or corrections, such as tests of normality and adjustment for multiple comparisons
☐	☒ A full description of the statistical parameters including central tendency (e.g. means) or other basic estimates (e.g. regression coefficient) AND variation (e.g. standard deviation) or associated estimates of uncertainty (e.g. confidence intervals)
☐	☒ For null hypothesis testing, the test statistic (e.g. *F*, *t*, *r*) with confidence intervals, effect sizes, degrees of freedom and *P* value noted *Give P values as exact values whenever suitable.*
☒	☐ For Bayesian analysis, information on the choice of priors and Markov chain Monte Carlo settings
☒	☐ For hierarchical and complex designs, identification of the appropriate level for tests and full reporting of outcomes
☒	☐ Estimates of effect sizes (e.g. Cohen's *d*, Pearson's *r*), indicating how they were calculated

Our web collection on statistics for biologists contains articles on many of the points above.

Software and code

Policy information about availability of computer code

Data collection	MetaMorph 7.7, XRTools software.
Data analysis	ImageJ 1.51w, ImageJ software version 1.51j8, ImageJ plugin KymoResliceWide v.0.4, custom-made JAVA plugin, ImageJ plugin DoM_Utrecht v.0.9.1, GraphPad Prism 7, Sigma-Plot software (Version 12.0), Trackmate plugin in Fiji (http://fiji.sc/TrackMate) were used for data anaylsis. All MATLAB and Mathematica notebooks used for computations, together with the raw data are available online [https://doi.org/10.6084/m9.figshare.7520033] and [https://github.com/RuddiRodriguez/Analysis-of-MT-plus-end-fluctuations].

For manuscripts utilizing custom algorithms or software that are central to the research but not yet described in published literature, software must be made available to editors/reviewers. We strongly encourage code deposition in a community repository (e.g. GitHub). See the Nature Research guidelines for submitting code & software for further information.

Data

Policy information about availability of data

All manuscripts must include a data availability statement. This statement should provide the following information, where applicable:

- Accession codes, unique identifiers, or web links for publicly available datasets
- A list of figures that have associated raw data
- A description of any restrictions on data availability

All data that support the conclusions are available from the authors on request, and/or available in the manuscript itself.

Field-specific reporting

Please select the one below that is the best fit for your research. If you are not sure, read the appropriate sections before making your selection.

☒ Life sciences ☐ Behavioural & social sciences ☐ Ecological, evolutionary & environmental sciences

For a reference copy of the document with all sections, see nature.com/documents/nr-reporting-summary-flat.pdf

Life sciences study design

All studies must disclose on these points even when the disclosure is negative.

Sample size	All experiments were independently repeated at least two and typically three or more times and each datasets were pooled across the experiments. No statistical methods were used to predetermine sample size. In each case, all replication numbers, sample sizes, statistical tests and P values are indicated in the figure legends and in method section. Sample size was chosen based on our previous experience and based on the standards in the field for measuring microtubule dynamics.
Data exclusions	No data were excluded.
Replication	All experiments were independently repeated at least two and typically three or more times. All attempts at replication were successful.
Randomization	For microtubule defect analysis, images from the -Fchitax-3 and +Fchitax-3 datasets collected by one team member were randomly mixed and were scored blindly by another team member
Blinding	For microtubule defect analysis, images from the -Fchitax-3 and +Fchitax-3 datasets collected by one team member were randomly mixed and were scored blindly by another team member. For rest of the data, blinding was not implemented because quantitative data were obtained through automated software or algorithms which are not human bias.

Reporting for specific materials, systems and methods

We require information from authors about some types of materials, experimental systems and methods used in many studies. Here, indicate whether each material, system or method listed is relevant to your study. If you are not sure if a list item applies to your research, read the appropriate section before selecting a response.

Materials & experimental systems

n/a	Involved in the study
☒	☐ Antibodies
☐	☒ Eukaryotic cell lines
☒	☐ Palaeontology
☒	☐ Animals and other organisms
☒	☐ Human research participants
☒	☐ Clinical data

Methods

n/a	Involved in the study
☒	☐ ChIP-seq
☒	☐ Flow cytometry
☒	☐ MRI-based neuroimaging

Eukaryotic cell lines

Policy information about cell lines

Cell line source(s)	HeLa (Kyoto) and human embryonic kidney 239T (HEK293T) cell lines were obtained from ATCC.
Authentication	ATCC performs short-tandem repeat profiling for cell line authentication, and no additional cell line authentication was performed.
Mycoplasma contamination	The cell line was routinely checked for mycoplasma contamination using LT07-518 Mycoalert assay.
Commonly misidentified lines (See ICLAC register)	The cell line used is not present in the list of commonly misidentified lines.